

ESC-TR-2002-077

Quarterly Technical Report

Solid State Research

2002:3

Lincoln Laboratory
MASSACHUSETTS INSTITUTE OF TECHNOLOGY
LEXINGTON, MASSACHUSETTS



Prepared for the Department of the Air Force under Contract F19628-00-C-0002.

Approved for public release; distribution is unlimited.

20030204 044

This report is based on studies performed at Lincoln Laboratory, a center for research operated by Massachusetts Institute of Technology. The work was sponsored by the Department of the Air Force under Contract F19628-00-C-0002.

This report may be reproduced to satisfy needs of U.S. Government agencies.

The ESC Public Affairs Office has reviewed this report, and it is releasable to the National Technical Information Service, where it will be available to the general public, including foreign nationals.

This technical report has been reviewed and is approved for publication.

FOR THE COMMANDER


Gary Tutungian
Administrative Contracting Officer
Plans and Programs Directorate
Contracted Support Management

Non-Lincoln Recipients

PLEASE DO NOT RETURN

Permission is given to destroy this document
when it is no longer needed.

Massachusetts Institute of Technology
Lincoln Laboratory

Solid State Research

**Quarterly Technical Report
2002:3**

1 May — 31 July 2002

Issued 29 January 2003

Approved for public release; distribution is unlimited.

Lexington

Massachusetts

ABSTRACT

This report covers in detail the research work of the Solid State Division at Lincoln Laboratory for the period 1 May through 31 July 2002. The topics covered are Quantum Electronics, Electro-optical Materials and Devices, Submicrometer Technology, Biosensor and Molecular Technologies, Advanced Imaging Technology, Analog Device Technology, and Advanced Silicon Technology. Funding is provided by several DoD organizations—including the Air Force, Army, DARPA, MDA, Navy, NSA, and OSD—and also by the DOE, NASA, and NIST.

**This Page Intentionally
Left Blank**

TABLE OF CONTENTS

Abstract	iii
List of Illustrations	vii
List of Tables	xi
Introduction	xiii
Reports on Solid State Research Organization	xv xxvii
1. QUANTUM ELECTRONICS	1
1.1 Miniature, High-Power 355-nm Laser System	1
2. ELECTRO-OPTICAL MATERIALS AND DEVICES	7
2.1 Silicon Microlens Fabrication by Mesa Etching and Mass-Transport Smoothing	7
3. SUBMICROMETER TECHNOLOGY	11
3.1 Prospects for Photolithography at 121 nm	11
4. BIOSENSOR AND MOLECULAR TECHNOLOGIES	19
4.1 EEL High-Energy Biofuel Cell	19
5. ADVANCED IMAGING TECHNOLOGY	23
5.1 Point-Spread Response of a Thick, Back-Illuminated CCD Imager	23
5.2 Radiation Effects on Avalanche Photodiodes	28

6.	ANALOG DEVICE TECHNOLOGY	35
6.1	Nonlinear Dielectric Microwave Losses in MgO Substrates	35
7.	ADVANCED SILICON TECHNOLOGY	43
7.1	"GRATEFUL" Phase Shift Lithography Method as a Cost-Effective Alternative for Low-Volume Lithography Needs	43

LIST OF ILLUSTRATIONS

Figure No.		Page
1-1	Schematic of miniature, high-power 355-nm laser system superimposed on mechanical drawing of housing (dimensions in inches).	1
1-2	Photograph of optical head of 355-nm laser system.	4
1-3	Output energy of laser head in the ir, green, and uv as a function of repetition rate.	5
1-4	Temporal profile of 355-nm pulse.	5
2-1	Scanning electron micrograph of Si microlens fabrication: (a) etched multi-mesa preform and (b) microlens formed after mass-transport smoothing.	8
2-2	Optical micrographs of (a) top view of mass-transported Si microlens and (b) image formed by microlens surface of the partially closed iris in the microscope. Note that the large ring of dark band in (a) is the graded sidewall of the etched well inside which the microlens is located.	8
2-3	Stylus surface-profiling trace of Si microlens [cf. Figure 2-2(a)].	9
3-1	Spectral output of hydrogen Lyman- α discharge lamp built by T. McCarthy and D. E. Murnick of Rutgers University.	12
3-2	Normalized thickness remaining vs incident 121-nm dose for four commercial resists.	15
3-3	Schematic of near-field contact mode photolithography with phase shift mask (upper left) and scanning electron micrographs of the 43-nm phase edges printed with such a mask.	16
3-4	Atomic force microscopy cross section of the photoresist lines, printed as shown in Figure 3-3.	17
4-1	EEL (Engineered Electrocyte Layers) biofuel cell. It should have high energy density, approximately 60 \times greater than batteries, and should be inexpensive to produce and refuel.	19
4-2	Genetic engineering of <i>Caulobacter</i> : (a) Test of protein targeting, (b) spliced genes, (c) <i>Caulobacter</i> with HfaD-GFP, as viewed with 400 \times fluorescent microscope (targeting still being optimized), and (d) adding stalk-tip proton pore.	20

LIST OF ILLUSTRATIONS (Continued)

Figure No.		Page
4-3	Maintenance of <i>Caulobacter</i> bacteria under typical biofuel cell conditions. (a) Bottom view of monolayer with 400× phase-contrast microscope, demonstrating that bacteria self-assemble into tightly packed monolayer. (b) Demonstration of constant number of live bacteria using NaN_3 or other growth inhibitors; growth when inhibitor is removed shows that bacteria are still alive.	22
5-1	Illustration of system for measuring the point-spread response of an image sensor to a light spot.	23
5-2	Surface plots of optical response of pixel to 430-nm light spot scanned over a $80 \times 80\text{-}\mu\text{m}$ subarray made (a) with two of the clock voltages at +4 V and the third at -6, and (b) with one phase at +0 V and two at -8 V. A grid depicting the pixel boundaries has been superimposed on the data.	24
5-3	Optical response to light spot scanned through the center of the pixel along and across the direction of the channel.	25
5-4	Depiction of scattering of near-ir light off surface features of a charge-coupled device (CCD). The illumination enters a back-illuminated device and is scattered (a) by the polysilicon-gates overlaps and (b) by the thick-oxide channel stops.	26
5-5	Surface plots of pixel response at 950 nm on devices (a) with and (b) without an Al film deposited over the CCD gates.	27
5-6	Operation of avalanche photodiode (APD) by arming to a reverse bias voltage above its breakdown threshold by means of a <i>p</i> -type field-effect transistor (FET).	28
5-7	Quenching of APD by switching on <i>n</i> -FET with its drain connected to APD cathode.	29
5-8	Three different reverse bias conditions at 100 K for irradiation of APDs. The APD breakdown voltage is ~25 V.	29
5-9	Circuit used in second set of irradiations in which APDs were actively armed and quenched to more closely emulate the electronic environment of integrated readout circuits.	31

LIST OF ILLUSTRATIONS (Continued)

Figure No.		Page
5-10	Circuit, microprobe, and cold wafer chuck used for measurements on APDs during the third irradiation experiment.	32
5-11	Pulsed dark count vs dc overbias potential for an APD irradiated with protons with its cathode held at high impedance.	32
5-12	Dark count rate vs dc overbias potential for an APD that was avalanching during irradiation with protons.	33
5-13	Pulsed dark count vs dc overbias potential for an APD before and after irradiation with x-rays.	33
6-1	Temperature-dependent effective surface resistance of YBCO film at $\omega/2\pi = 2.3$ GHz for two input power levels (-60 dBm, open triangles; -20 dBm, circles), corresponding to $E_{rf} \sim 0.5$ and 10^4 V/m. Note the logarithmic scales for illustration. The inset shows the normalized R_{eff} vs input power for the YBCO film (diamonds) and a Nb film on MgO (triangles) at $T = 5$ K. The absolute values of R_{eff} of both samples at 1.7 K were identical.	36
6-2	Typical data for shift of surface reactance at 2.3 GHz for YBCO on MgO at temperatures below 20 K for power levels shown in Figure 6-1 that give maximum change in effective surface resistance (-60 dBm, triangles; -20 dBm, circles).	37
6-3	Temperature-dependent (a) dielectric loss tangent and (b) permittivity at $f = 2.3$ GHz for YBCO on MgO (-60 dBm, triangles, dotted interpolation; -20 dBm, circles, solid interpolation) and Nb on MgO (various power levels, diamonds, dashed interpolation), as expected for resonant absorption. $T_0 = 5.2$ K. The $\Delta X_{eff}(T)$ data for Nb were corrected for the temperature variation of the superconducting penetration depth according to the BCS theory ($T_c = 9.2$ K, $\Delta(0)/kT_c = 1.8$).	39
6-4	Electric field-induced variation of the effective surface resistance for YBaCuO (circles) and Nb (diamonds) on MgO at $f = 2.3$ GHz and $T = 5$ K. The dashed and solid curves denote fits to Equation (6.6).	40

LIST OF ILLUSTRATIONS (Continued)

Figure No.		Page
7-1	Schematic diagram of the GRATEFUL imaging method: (a) horizontal phase shift and trim masks, (b) simulated first resist image (relative total exposure dose), (c) vertical phase shift and trim masks, (d) simulated second resist image (relative total exposure dose), and (e) geometric union of horizontal and vertical resist features (simple resist threshold model). Simple phase shift template masks are used for the fine feature definitions.	44
7-2	Experimental example of circuit pattern imaged using GRATEFUL. All the fine features are in one orientation in this example so only three exposures were required. Note the absence of optical proximity effects for these 65-nm gate features imaged through pitch values of 250 nm to isolated.	44
7-3	Experimental example of two-dimensional test pattern imaged using GRATEFUL. The x -oriented features are 85 nm and the y -oriented features 125 nm. Note the sharp corners achieved through the use of two optically independent resist layers.	45
7-4	Two-dimensional grid pattern fabricated in two layers of resist. Such a method is capable of producing very sharp corner features for low values of k_1 . The grating pitch value is 280 nm in this case.	46
7-5	Simulated thresholded aerial image plot of a full adder circuit implemented using GRATEFUL. This implements a $k_1 = 0.3$ lithography process for our Canon EX-4, 248-nm stepper with numerical aperture 0.6. Simulations were performed using Numerical Technologies' IC Workbench software.	46
7-6	Experimental example of full adder circuit region imaged using GRATEFUL. Note the fine features oriented in x and y directions imaged using the same one-dimensional phase shift mask grating.	47

LIST OF TABLES

Table No.		Page
3-1	121-nm Absorption Coefficients and Maximum Thickness for Optical Density 0.4 of Several Polymers Relevant to Photoresist Process and of Several Commercial Resists Used for Higher-Wavelength Lithography	14
5-1	Dark Count Rate of APDs Before and After Proton Irradiation at 100 K	30
5-2	Dark Count Rate of Irradiated APDs After Room-Temperature Annealing	30

**This Page Intentionally
Left Blank**

INTRODUCTION

1. QUANTUM ELECTRONICS

A robust, miniature laser system has produced 100- μ J, 355-nm pulses of 700-ps duration at pulse rates up to 500 Hz. The system is pumped by two fiber-coupled 808-nm laser diode arrays and occupies a volume of <0.5 liters.

2. ELECTRO-OPTICAL MATERIALS AND DEVICES

High-quality Si microlenses have been fabricated by preform mesa etching and subsequent mass-transport smoothing. The surface-energy process is analogous to that established in III-V compounds, and the microlenses are promising for many microoptical applications.

3. SUBMICROMETER TECHNOLOGY

An experimental optical lithography system, using phase shift masking and a 121-nm exposure wavelength, has successfully printed 43-nm-wide isolated features. Candidate resist materials and exposure sources have been identified for use in a practical commercial lithography system.

4. BIOSENSOR AND MOLECULAR TECHNOLOGIES

Novel biofuel cells are being developed that use genetically engineered bacteria. These fuel cells should have energy densities up to 60 \times greater than conventional batteries, and they could be refueled using almost any form of organic matter.

5. ADVANCED IMAGING TECHNOLOGY

The response of 40–50- μ m-thick, back-illuminated charge-coupled devices to a scanned optical spot has been measured at blue and near-ir wavelengths, and the results indicate that the device is fully depleted with good point-spread response. However, in the near-ir where the radiation penetrates through to the front surface, evidence exists of optical scattering off device surface features (channel stops and poly-gates) that enhances the crosstalk in nearby pixels.

The effects of radiation damage on front-illuminated silicon avalanche photodiodes operating under differing bias conditions have been investigated. The effect of radiation damage, which appears to be due to ionizing radiation, is minimized by reducing the bias on the devices or allowing them to float electrically.

6. ANALOG DEVICE TECHNOLOGY

The nonlinear surface impedance and two-tone intermodulation distortion of nine epitaxial $\text{YBa}_2\text{Cu}_3\text{O}_{7-\delta}$ and several Nb films on MgO substrates have been investigated, using stripline resonators, at

frequencies $f = 2.3\text{--}11.2$ GHz and temperatures $T = 1.7$ K to T_c . The power dissipation decreased by up to one order of magnitude as the microwave electric field was increased to about 100 V/m for $T < 20$ K; this anomalous response results from dielectric losses in MgO due to defect dipole relaxation.

7. ADVANCED SILICON TECHNOLOGY

The application of multiple exposure strong phase shift lithography to fully scaled low-volume circuit patterns has been explored, using a dense-only patterning method dubbed "GRATEFUL" (Gratings of Regular Arrays and Trim Exposures For ULSI Lithography). The method sacrifices process complexity and design flexibility in exchange for dramatically lower mask cost and minimized optical proximity and related spatial frequency effects.

REPORTS ON SOLID STATE RESEARCH
1 MAY THROUGH 31 JULY 2002

PUBLICATIONS

Low-Energy Electron-Excited
Nanoluminescence Studies of GaN
and Related Materials

L. J. Brillson*
S. T. Bradley*
S. H. Goss*
X. Sun*
M. J. Murphy*
W. J. Schaff*
L. F. Eastman*
D. C. Look*
R. J. Molnar
F. A. Ponce*
N. Ikeo*

Appl. Surf. Sci. **190**, 498 (2002)

Substrate Preparation and Low-
Temperature Boron Doped Silicon
Growth on Wafer-Scale Charge-
Coupled Devices by Molecular
Beam Epitaxy

S. D. Calawa
B. E. Burke
P. M. Nitishin
A. H. Loomis
J. A. Gregory
T. A. Lind

J. Vac. Sci. Technol. B **20**, 1170
(2002)

Magnetoelastic Effects of Iron-
Group Ions in Exchange Fields

G. F. Dionne

J. Appl. Phys. **91**, 7367 (2002)

Direct Imaging of Reverse-Bias
Leakage Through Pure Screw
Dislocations in GaN Films Grown
by Molecular Beam Epitaxy on
GaN Templates

J. W. P. Hsu*
M. J. Manfra
R. J. Molnar
B. Heying*
J. S. Speck*

Appl. Phys. Lett. **81**, 79 (2002)

*Author not at Lincoln Laboratory.

- High Mobility AlGaIn/GaN
Heterostructures Grown by Plasma-
Assisted Molecular Beam Epitaxy
on Semi-Insulating GaN Templates
Prepared by Hydride Vapor Phase
Epitaxy
- M. J. Manfra
N. G. Weimann*
J. W. P. Hsu*
L. N. Pfeiffer*
K. W. West*
S. Syed*
H. L. Stormer*
W. Pan*
D. V. Lang*
S. N. G. Chu*
G. Kowach*
- J. Appl. Phys.* **92**, 338 (2002)
- Cold Cathode Microwave Devices
- R. A. Murphy
M. A. Kodis*
- In Vacuum Microelectronics*
(Wiley, New York, 2001), pp.
349-391
- Deep Hole Traps in *n*-GaIn Films
Grown by Hydride Vapor Phase
Epitaxy
- A. Y. Polyakov*
N. B. Smirnov*
A. V. Govorkov*
Z-Q. Fang*
D. C. Look*
R. J. Molnar
A. V. Osinsky*
- J. Appl. Phys.* **91**, 6580 (2002)
- Single Frequency 1550-nm
AlGaInAs-InP Tapered High-Power
Laser with a Distributed Bragg
Reflector
- S. R. Selmic*
G. A. Evans*
T. M. Chou*
J. B. Kirk*
J. N. Walpole
J. P. Donnelly
C. T. Harris
L. J. Missaggia
- IEEE Photon. Technol. Lett.*
14, 890 (2002)
- Scanning Kelvin Probe Microscopy
of Surface Electronic Structure in
GaIn Grown by Hydride Vapor
Phase Epitaxy
- B. S. Simpkins*
D. M. Schaadt*
E. T. Yu*
R. J. Molnar
- J. Appl. Phys.* **91**, 9924 (2002)

*Author not at Lincoln Laboratory.

Depth-Dependent Investigation of Defects and Impurity Doping in GaN/Sapphire Using Scanning Electron Microscopy and Cathodoluminescence Spectroscopy

X. L. Sun*
S. H. Goss*
L. J. Brillson*
D. C. Look*
R. J. Molnar

J. Appl. Phys. **91**, 6729 (2002)

Slab-Coupled 1.3- μm Semiconductor Laser with Single-Spatial Large-Diameter Mode

J. N. Walpole
J. P. Donnelly
P. J. Taylor
L. J. Missaggia
C. T. Harris
R. J. Bailey
A. Napoleone
S. H. Groves
S. R. Chinn
R. Huang
J. J. Plant

IEEE Photon. Technol. Lett. **14**, 756 (2002)

PRESENTATIONS[†]

Sample Preparation Protocols for Rapid, Simple Extraction and Identification of DNA in Environmental Samples

L. Parameswaran
L. Bortlin
J. Bobrow
J. Harper

Biodetection Technologies Knowledge Foundation Conference, Alexandria, Virginia, 1-3 May 2002

Progress in Implementing a Superconductive Type-II Quantum Computer

K. K. Berggren
J. Sage
P. Cho
E. Macedo
R. Slattery
T. Weir
D. Nakada*
D. Berns*
T. P. Orlando*

Quantum Computing for Physical Modeling, Martha's Vineyard, Massachusetts, 6-9 May 2002

*Author not at Lincoln Laboratory.

[†] Titles of presentations are listed for information only. No copies are available for distribution.

Architectures for Superconductive Type-II Quantum Computers	J. Sage K. K. Berggren T. P. Orlando* D. Berns*	Quantum Computing for Physical Modeling, Martha's Vineyard, Massachusetts, 6-9 May 2002
Contamination of Optical Surfaces at 157 nm	T. M. Bloomstein S. T. Palmacci D. E. Hardy J. H. C. Sedlacek V. Liberman M. Rothschild	157-nm Data Review, Dallas, Texas, 7-9 May 2002
Antimony-Based III-V Materials Grown by OMVPE for Thermophotovoltaics and Lasers	C. A. Wang	14th International Conference on InP, Stockholm, Sweden, 12-16 May 2002
Intelligent Multi-Mode Multiband RF Amplifiers	M. Gouker C. Keast A. Anderson	Intelligent RF Front End Kickoff Meeting, Hilton Head, South Carolina, 13-16 May 2002
CANARY B-Cell Sensor for Rapid Identification of Pathogens	M. Petrovick	102nd General Meeting of the American Society for Microbiology, Salt Lake City, Utah, 19-23 May 2002
Wavelength Beam Combining of Ytterbium Fiber Lasers in a MOPA Configuration	S. J. Augst A. K. Goyal R. L. Aggarwal T. Y. Fan A. Sanchez	Conference on Lasers and Electro-Optics/Quantum Electronics and Laser Science Conferences, Long Beach, California, 19-24 May 2002

*Author not at Lincoln Laboratory.

Impact of Photodetector
Nonlinearities on Photonic Analog-
to-Digital Converters

J. J. Hargreaves
J. C. Twichell

Conference on Lasers and
Electro-Optics/Quantum
Electronics and Laser Science
Conferences,
Long Beach, California,
19-24 May 2002

Impact of Photodiode
Nonlinearities on Photonic Analog-
to-Digital Converters

P. W. Juodawlkis
F. J. O'Donnell
J. J. Hargreaves
D. C. Oakley
A. Napoleone
S. H. Groves
L. J. Mahoney
K. M. Molvar
L. J. Missaggia
J. P. Donnelly
J. C. Twichell

Conference on Lasers and
Electro-Optics/Quantum
Electronics and Laser Science
Conferences,
Long Beach, California,
19-24 May 2002

Miniature, Pulsed Ti-Sapphire
Laser System

J. J. Zayhowski
A. L. Wilson

Conference on Lasers and
Electro-Optics/Quantum
Electronics and Laser Science
Conferences,
Long Beach, California,
19-24 May 2002

Miniature Short-Pulsed Lasers

J. J. Zayhowski

Technical Presentation,
Leica Geosystems,
Napa, California,
24 May 2002

Photospeed Considerations for
Extreme Ultraviolet Lithography
Resists

P. M. Dentinger*
L. L. Hunter*
D. J. O'Connell*
S. Gunn*
D. Goods*
T. H. Fedynyshyn
R. B. Goodman
D. K. Astolfi

46th International Conference
on Electron, Ion, Photon Beam
Technology and
Nanofabrication,
Anaheim, California,
28-31 May 2002

Optical Imaging Properties of
Dense Phase-Shift Feature Patterns

M. Fritze
B. Tyrrell
R. Mallen
B. Wheeler

46th International Conference
on Electron, Ion, Photon Beam
Technology and
Nanofabrication,
Anaheim, California,
28-31 May 2002

Prospects for Photolithography at
121 nm

V. Liberman
M. Rothschild
P. G. Murphy
S. T. Palmacci

46th International Conference
on Electron, Ion, Photon Beam
Technology and
Nanofabrication,
Anaheim, California,
28-31 May 2002

A High-Power MEMS Electrostatic
Induction Motor

C. Livermore*
A. Forte
T. Lyszczarz
S. D. Umans*
J. H. Lang*

2002 Solid-State Sensor,
Actuator and Microsystems
Workshop,
Hilton Head, South Carolina,
2-6 June 2002

MIT Lincoln Laboratory Capacitive
Switch: Technology, Reliability
and Packaging

C. L. Keast
J. B. Muldavin
S. R. Berry
C. O. Bozler
M. A. Gouker
J. F. Howard
J. M. Knecht
S. Rabe
L. Travis

IEEE MTT-S International
Microsystems Symposium,
Seattle, Washington,
2-7 June 2002

*Author not at Lincoln Laboratory.

Static and Dynamic Modeling of
RF MEMS Switches

J. B. Muldavin
C. L. Keast
C. O. Bozler
S. R. Berry

IEEE MTT-S International
Microsystems Symposium,
Seattle, Washington,
2-7 June 2002

Tunable Devices at Cryogenic
Temperatures

D. E. Oates

IEEE MTT-S International
Microsystems Symposium,
Seattle, Washington,
2-7 June 2002

Tunable Superconducting Filters

D. E. Oates

IEEE MTT-S International
Microsystems Symposium,
Seattle, Washington,
2-7 June 2002

Wavelength Beam Combining of
Ytterbium Fiber Lasers

S. J. Augst
A. K. Goyal
R. L. Aggarwal
T. Y. Fan
A. Sanchez

Solid State Diode Laser
Technology Review,
Albuquerque, New Mexico,
3-7 June 2002

Wavelength Beam Combining of
Aluminum-Free, Mid-IR
Semiconductor Lasers

A. K. Goyal
A. Sanchez
G. W. Turner
T. Y. Fan
Z. L. Liao
M. J. Manfra
P. J. Foti
L. J. Missaggia
P. O'Brien
J. L. Daneu

Solid State Diode Laser
Technology Review,
Albuquerque, New Mexico,
3-7 June 2002

Slab-Coupled Semiconductor
Lasers with Single-Spatial, Large-
Diameter Mode

R. K. Huang
J. P. Donnelly
L. J. Missaggia

Solid State Diode Laser
Technology Review,
Albuquerque, New Mexico,
3-7 June 2002

Recent Progress in Optically
Pumped, Aluminum-Free Mid-IR
Semiconductor Lasers Based on
Integrated Absorber Designs

G. W. Turner
A. K. Goyal
M. J. Manfra
P. J. Foti
A. Sanchez

Solid State Diode Laser
Technology Review,
Albuquerque, New Mexico,
3-7 June 2002

Tunable Superconducting Filters

D. E. Oates

Symposium on High T_c
Superconductors in High
Frequency Fields,
Woods Hole, Massachusetts,
10-12 June 2002

Nonlinear Surface Impedance of
High Temperature Superconductor
Films

D. E. Oates
D. Agassi*

Symposium on High T_c
Superconductors in High
Frequency Fields,
Woods Hole, Massachusetts,
10-12 June 2002

Doping-Dependent Nonlinear
Microwave Response of Epitaxial
YBaCuO Films

D. E. Oates
S-H. Park
D. Seron*
M. A. Hein*
P. J. Hirst*
R. G. Humphreys*
G. Koren*
E. Polturak*

Symposium on High T_c
Superconductors in High
Frequency Fields,
Woods Hole, Massachusetts,
10-12 June 2002

Subwavelength Optical Lithography
Using Resolution Enhancements

M. Fritz

American Vacuum Society,
New England Chapter Meeting,
Burlington, Massachusetts,
10-14 June 2002

*Author not at Lincoln Laboratory.

Progress in Semiconductor
Reference Oscillator Development
for Coherent Detection Optical
Remote Sensing

G. W. Turner
M. J. Manfra
D. M. Tratt*
K. Mansour*
R. T. Menzies*
P. D. Maker*
R. J. Chacon*
R. E. Muller*

2nd Annual Earth Science
Technology Conference,
Pasadena, California,
11-13 June 2002

Contamination of Optical Surfaces
at 157 nm

T. M. Bloomstein
S. T. Palmacci
D. E. Hardy
J. H. C. Sedlacek
V. Liberman
M. Rothschild

Contamination Control and
Monitoring Roadmap for
Lithography Workshop,
Newport, Rhode Island,
16-17 June 2002

Broadband (200–1000 nm) Back-
Illuminated CCD Imagers

B. E. Burke
J. A. Gregory
A. H. Loomis
S. D. Calawa
P. M. Nitishin
T. A. Lind
M. J. Cooper
D. J. Young
P. W. O'Brien
B. B. Kosicki
G. A. Luppino*
J. L. Tonry*

Scientific Detectors for
Astronomy Workshop,
Waimea, Hawaii,
16-22 June 2002

The Orthogonal Parallel Transfer
Imaging Camera

B. E. Burke
J. L. Tonry*
G. A. Luppino*
N. Kaiser*

Scientific Detectors for
Astronomy Workshop,
Waimea, Hawaii,
16-22 June 2002

*Author not at Lincoln Laboratory.

Giga-Pixels and Sky Surveys	B. E. Burke J. L. Tonry* G. A. Luppino* N. Kaiser* G. H. Jacoby*	Scientific Detectors for Astronomy Workshop, Waimca, Hawaii, 16-22 June 2002
A CCD Based Curvature Based Wavefront Sensor for Adaptive Optics: Laboratory Results	R. J. Dorn* B. E. Burke J. W. Beletic*	Scientific Detectors for Astronomy Workshop, Waimca, Hawaii, 16-22 June 2002
Silicon on Insulator-Based Single- Chip Image Sensors	V. Suntharalingam B. Burke M. Cooper	Scientific Detectors for Astronomy Workshop, Waimca, Hawaii, 16-22 June 2002
Prospects for Photolithography at 121 nm	V. Liberman M. Rothschild P. G. Murphy S. T. Palmacci	Technical Seminar, Semiconductor Leading Edge Technologies (Selete), Tokyo, Japan, 24 June 2002
“Dense Only” Phase Shift Template Lithography	M. Fritze B. Tyrrell	8th Annual Advanced Reticle Symposium, San Jose, California, 25 June 2002
Reduction of the Interface Recombination Rate in GaInAsSb/ GaSb Broken-Gap Heterostructures	C. A. Wang D. Donetsky* S. Anikeev* G. Belenky* S. Luryi* G. Nichols*	Electronic Materials Conference, Santa Barbara, California, 26-28 June 2002

*Author not at Lincoln Laboratory.

Fluoroaromatic Resists for 157 nm
Lithography

T. H. Fedynyshyn
R. R. Kunz
R. F. Sinta
M. Sworin
W. A. Mowers
R. B. Goodman
A. Cabral

Photopolymer Science and
Technology Conference,
Tokyo, Japan,
26-29 June 2002

Introducing the Passive Anode
Surface Emission Cathode

D. Cooke*
M. W. Geis

American Institute of
Aeronautics and Astronautics
Joint Propulsion Conference,
Indianapolis, Indiana,
5 July 2002

High-Speed, Electronically
Shuttered Solid-State Imager
Technology

R. K. Reich
D. D. Rathman
D. M. O'Mara
D. J. Young
A. H. Loomis
E. J. Kohler
R. M. Osgood
R. A. Murphy
M. Rose
R. Berger
S. A. Watson*
M. D. Ulibarri*
T. Perry*
B. B. Kosicki

14th Topical Conference on
High Temperature Plasma
Diagnostics,
Madison, Wisconsin,
8-11 July 2002

Multifocal Multiphoton Microscopy
(MMM) at a Framerate in Excess of
500 Hz

R. K. Reich
B. B. Kosicki
W. H. McGonagle
K. Bahlmann*
P. So*
M. Kirber*
K. Bellve*

Gordon Research Conference:
Lasers in Medicine and
Biology,
Meriden, New Hampshire,
14-19 July 2002

*Author not at Lincoln Laboratory.

Coupling of Single Mode Fibers to
Planar SI Waveguides Using
Vertically Tapered Mode Converters

C. Bozler
C. Keast
J. Knecht
R. Williamson
M. Fritze
M. B. Frish*
J. A. Fijol*
E. E. Fike*
S. A. Jacobson*
P. B. Keating*
W. J. Kessler
J. LeBlanc*

Optical Society of America
Integrated Photonics Research
Topical Meeting,
Vancouver, British Columbia,
Canada,
17-19 July 2002

Superconductive Device
Fabrication and Development

K. Berggren
J. Sage
E. Macedo
R. Slattery

Defense University Research
Initiative on NanoTechnology
(DURINT) Review,
Massachusetts Institute of
Technology,
Cambridge, Massachusetts,
29-30 July 2002

Slab-Coupled Semiconductor
Lasers with Single-Spatial, Large-
Diameter Mode

J. P. Donnelly
R. K. Huang
J. M. Walpole*
L. J. Missaggia
C. T. Harris
R. J. Bailey
J. Plant
D. E. Mull
W. D. Goodhue
P. J. Taylor
A. Napolcon
G. W. Turner

SPIE ITCOM: Communication
Networking, Computing, and
Storage Technologies and
Applications,
Boston Massachusetts,
29 July-1 August 2002

*Author not at Lincoln Laboratory.

ORGANIZATION

SOLID STATE DIVISION

D. C. Shaver, Head
R. W. Ralston, Associate Head
N. L. DeMeo, Jr., Assistant
Z. J. Lemnios, Senior Staff
J. W. Caunt, Assistant Staff
K. J. Challberg, Administrative Staff
J. D. Pendergast, Administrative Staff

SUBMICROMETER TECHNOLOGY

M. Rothschild, Leader
T. M. Lyszczarz, Assistant Leader
T. H. Fedynyshyn, Senior Staff
R. R. Kunz, Senior Staff

Astolfi, D. K.	Lennon, D. M.
Bloomstein, T. M.	Lieberman, V.
Cann, S. G.	Mowers, W. A.
DiNatale, W. F.	Palmacci, S. T.
Efremow, N. N., Jr.	Sedlacek, J. H. C.
Geis, M. W.	Spector, S. J.
Goodman, R. B.	Switkes, M.
Krohn, K. E.	Sworin, M.
Leibowitz, F. L.	Yoon, J. U.

QUANTUM ELECTRONICS

A. Sanchez-Rubio, Leader
T. Y. Fan, Assistant Leader
T. H. Jeys, Senior Staff
J. J. Zayhowski, Senior Staff

Aggarwal, R. L.	Hybl, J. D.
Augst, S. J.	Lynch, E. J.
Daneu, J. L.	O'Brien, P. W.
Daneu, V.	Ochoa, J. R.
Goyal, A. K.	Ripin, D. J.
Herzog, W. D.	

ELECTRO-OPTICAL MATERIALS AND DEVICES

J. C. Twichell, Leader
G. W. Turner, Assistant Leader
D. L. Spears, Senior Staff
C. A. Wang, Senior Staff
R. C. Williamson, Senior Staff

Bailey, R. J.	Harris, C. T.	Mull, D. E.
Betts, G. E.	Huang, R. K.	Napoleone, A.
Calawa, D. R.	Juodawlkis, P. W.	Nitishin, P. M.
Calawa, S. D.	LaForge, B. E.	Oakley, D. C.
Connors, M. K.	Liau, Z. L.	O'Donnell, F. J.
Donnelly, J. P.	Mahoney, L. J.	Plant, J. J.
Goodhue, W. D.	Manfra, M. J.	Shiau, D. A.
Groves, S. H.	McIntosh, K. A.	Taylor, P. J.
Hargreaves, J. J.	Missaggia, L. J.	Younger, R. D.
Harman, T. C.	Molnar, R. J.	

BIOSENSOR AND MOLECULAR
TECHNOLOGIES

M. A. Hollis, Leader
T. H. Rider, Senior Staff

Blanchard, D. J.	Nargi, F. E.
Cabrera, C. R.	Parameswaran, L.
Filip, L. C.	Petrovick, M. S.
Graves, C. A.	Postema-Zook, C. E.
Harper, J. D.	Schmidt, T. L.
Lakdawala, S.	Schwoebel, E. D.
Mathews, R. H.	

ANALOG DEVICE TECHNOLOGY

M. A. Gouker, Leader
L. M. Johnson, Assistant Leader
A. C. Anderson, Senior Staff

Berggren, K. K.	Oates, D. E.
Boisvert, R. R.	Sage, J. P.
Fitch, G. L.	Santiago, D. D.
Lyons, W. G.	Seaver, M. M.
Macedo, E. M., Jr.	Slattery, R. L.
Murphy, P. G.	Weir, T. J.

ADVANCED IMAGING TECHNOLOGY

B. B. Kosicki, Leader
R. K. Reich, Assistant Leader
B. E. Burke, Senior Staff

Aull, B. F.	Loomis, A. H.
Ciampi, J. S.	Mallen, R. D.
Cooper, M. J.	McGonagle, W. H.
Craig, D. M.	O'Mara, D. M.
Daniels, P. J.	Osgood, R. M.
Doherty, C. L., Jr.	Percival, K. A.
Dolat, V. S.	Rathman, D. D.
Felton, B. J.	Rose, M. K.
Gregory, J. A.	Stern, A.
Johnson, K. F.	Young, D. J.
Lind, T. A.	

ADVANCED SILICON TECHNOLOGY

C. L. Keast, Leader
V. Suntharalingam, Assistant Leader
P. W. Wyatt, Senior Staff

Austin, E. E.	Muldavin, J. B.
Berger, R.	Newcomb, K. L.
Bozler, C. O.	Rabe, S.
Burns, J. A.	Soares, A. M.
Chen, C. K.	Travis, L.
Chen, C. L.	Tyrrell, B. M.
D'Onofrio, R. P.	Warner, K.
Fritze, M.	Wheeler, B. D.
Gouker, P. M.	Yost, D.-R.
Healey, R. E.	Young, G. R.
Knecht, J. M.	

1. QUANTUM ELECTRONICS

1.1 MINIATURE, HIGH-POWER 355-nm LASER SYSTEM

The 450- μJ output of an amplified, 1064-nm passively Q -switched microchip laser is frequency tripled to 355 nm with 25% efficiency at pulse repetition rates up to 500 Hz in a robust, miniature system. The turnkey system was designed to survive temperature excursions from -40 to 71°C , shocks in excess of 20 G, and the vibrations encountered in demanding flight scenarios.

A schematic of the laser system is shown in Figure 1-1. It is pumped with two fiber-coupled diode laser arrays and occupies a volume of <0.5 liters. This system uses many of the components and techniques used in the miniature Ti:Sapphire laser system recently reported [1]. In this report, we walk the reader through the system and summarize its performance.

The first stage of the laser system is a passively Q -switched Nd:YAG microchip laser [2]–[5]. The microchip laser is pulse pumped with a fiber-coupled diode laser array; the diodes are turned on and off by a digital clock. The output of the pump fiber passes through a protective window and is imaged in the microchip laser with an aspheric doublet. The output of the microchip laser passes through two Brewster-angle glass plates and a beam positioner, and is then collimated.

The pump diode array is rated at 25-W cw and operated at a derated peak power of 12 W, with a pump-pulse duration of 300 μs . It is coupled to the laser head via a jacketed optical fiber with a core diameter of 200 μm and a 0.22 numerical aperture. The output of the fiber enters the environmentally

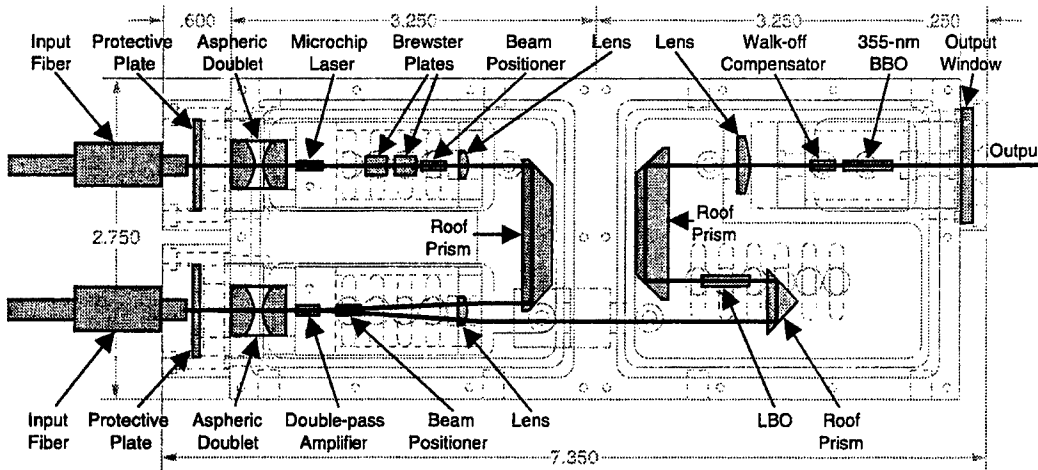


Figure 1-1. Schematic of miniature, high-power 355-nm laser system superimposed on mechanical drawing of housing (dimensions in inches).

sealed laser head through a window coated to be antireflecting at the 808-nm diode wavelength and highly reflecting at 1064 and 532 nm. It is then focused into the microchip laser with an aspheric doublet, with a nominal magnification of 0.5. The actual magnification is fixed by adjusting the position of the lens to optimize the performance of the microchip laser.

The microchip laser is 6.5 mm long. It is a composite of four crystals: a 1-mm-long Cr^{3+} :YAG input endcap, a 3-mm-long Nd^{3+} : Cr^{3+} :YAG gain section, a 1.5-mm-long Cr^{4+} :YAG saturable absorber, and a 1-mm-long Cr^{3+} :YAG output endcap. The Nd^{3+} : Cr^{3+} :YAG is doped at 1.4 wt% Nd; the Cr^{4+} :YAG has an unsaturated absorption coefficient of 6 cm^{-1} at 1064 nm. The Cr^{3+} doping is used to make the YAG radiation hard [6] — it serves no optical purpose. The two faces of the microchip laser are flat and parallel. The input face is antireflection (AR) coated at the pump wavelength and highly reflecting at the oscillating wavelength, 1064 nm; the output face is 40% reflecting at 1064 nm. Similar passively Q -switched microchip lasers, without the Cr^{3+} doping, have been reported elsewhere [3]–[5].

The microchip laser is heatsunk on the top and bottom. The thermal gradients and stress from mounting the top heat sink help fix the eigenpolarizations of the oscillating mode. The output of the laser passes through two Brewster plates and a beam positioner before being collimated with a 30-mm-focal-length lens.

Although the top heat sink fixes the eigenpolarizations of the system, the laser can oscillate in either the vertical (perpendicular to the base) or horizontal polarization. The thermal gradients favor oscillation in the vertical mode. At the low repetition rates that this system is intended for, the polarization selection is weak and, without the Brewster plates, very small amounts of feedback can cause polarization hopping. By controlling the polarization of the external feedback during the early formation of the pulse, particularly when the amplifier is on, the Brewster plates stabilize the polarization of the oscillating mode. In effect, they fix the polarization of the seed pulse that results from the feedback.

The beam positioner is critical to our ability to align the total system, and is used in several places. It consists of a 5-mm-long piece of YAG with flat and parallel input and output faces. The AR-coated crystal is mounted in a machined ball bearing that sits in a socket in the submount. As we rotate the ball bearing, the refraction of the YAG translates the output beam vertically or horizontally. When the beam positioner is located before a lens, we can use this mechanism to precisely control the pointing of the laser. Once the beam positioner is in the proper position, we pot the ball bearing in place and remove the alignment stick. We use the same arrangement to align the Brewster plates and the nonlinear optics later in the system, since it allows us to rotate crystals in all three directions without moving the center of the crystal, to facilitate proper phase matching.

The passively Q -switched microchip laser produces $65 \mu\text{J}$ in a 650-ps pulse, in a TEM_{00} beam. The collimated output goes through a roof prism and enters the amplifier stage of the device.

The output of the microchip laser enters the amplifier stage through the lens that is later used to collimate the output of the amplifier. The beam enters the stage ~ 1.5 mm off axis; the output of the amplifier is ~ 2.0 mm to the opposite side of the axis. The exact position of the beam is controlled by the placement of the roof prism. The beam positioner in the microchip laser stage is used to ensure that the

beam enters the amplifier stage propagating in a direction parallel to the axis of the amplifier submount (before the lens). A small tilt of the amplifier on its submount helps reduce feedback to the laser and results in the small asymmetry in the position of the incoming and outgoing beam. The 30-mm lens focuses the input beam into the amplifier. A beam positioner, placed within a few millimeters of the amplifier, is used to obtain maximum overlap of the incoming beam and the pumped region of the amplifier.

The amplifier is a 4.5-mm-long composite of three crystals: a passive 0.5-mm-long YAG pump-side endcap, a 3-mm-long Nd^{3+} :YAG gain section, and a passive 1-mm-long YAG output endcap. The two faces of the amplifier are flat, with a 2.5-min wedge between them. The pump-side face is AR coated at the pump wavelength and highly reflecting at 1064 nm; the output facet is antireflecting at 1064 nm. After making a double pass through the amplifier, the laser beam goes back through the beam positioner and is recollimated.

To simplify the system, the pump diodes for the amplifier were slaved to the pump diodes for the Q-switched laser, so that both arrays are on at the same time. The 300- μs pump period was chosen to obtain maximum inversion in the amplifier; the microchip laser pump power was then selected to optimize the performance of the laser given the long pump period. The amplifier pump diodes are operated near their maximum rated power, at 23 W, to provide the highest gain in the amplifier. Increasing the pump power beyond this point no longer increases the output power of the amplifier [1]. The optical train used to pump the amplifier is similar to that used to pump the microchip laser. At 500 Hz the output of the amplifier has a pulse energy of 450 μJ and is near diffraction limited.

The (nominally) collimated output of the amplifier enters the frequency-doubling stage through a small roof prism. The ir light is frequency doubled in a 10-mm-long piece of LBO, oriented for type-I phase matching. (LBO has the benefit of being radiation hard [7]). The LBO gives a maximum second-harmonic conversion efficiency of 50%, producing >200 μJ per pulse in a smooth, nearly Gaussian, green beam.

With the saturated spatial and temporal profile of the ir beam that results from efficient frequency doubling, equal amounts of ir and green light are not the optimal balance for efficient third-harmonic generation in this system. To optimize the color balance, we take advantage of the temperature sensitivity of harmonic conversion in LBO. The LBO is optimized for second-harmonic conversion at the nominal, uncontrolled room temperature. A thermistor is mounted directly on the LBO. Thermoelectric coolers are used to control the temperature of the laser head, as measured on the LBO. Optimal uv generation is obtained at $\sim 1^\circ\text{C}$ below the optimal temperature for green conversion, corresponding to a mix of 45% green light and 55% ir light incident on the BBO crystal.

On their way to the final nonlinear stage, the ir and green output of the LBO pass through another roof prism and are collimated with a 100-mm-focal-length lens. At this point, the diameters of the ir and green beams are $\sim 500 \mu\text{m}$. Summing of the fundamental and second-harmonic beams is performed in a 10-mm-long piece of BBO, oriented for type-II phase matching.

Over the length of the BBO, the ir and generated uv light walk off from the green light by $\sim 750 \mu\text{m}$, in the vertical direction. To compensate for this, a 5-mm-long piece of BBO is placed in the beam before

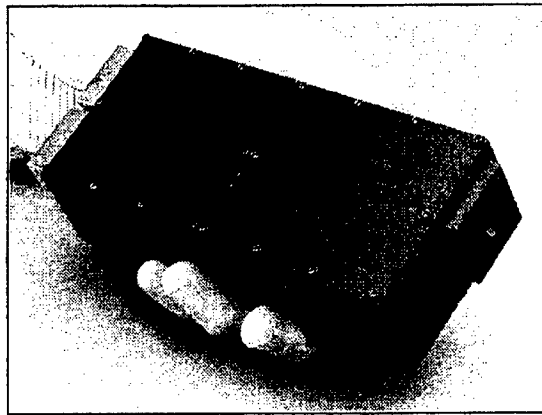


Figure 1-2. Photograph of optical head of 355-nm laser system.

the third-harmonic crystal. The shorter piece of BBO is cut off of the third-harmonic phase-matching direction; it generates no uv. It is aligned so that the ir light walks off from the green light by $\sim 325 \mu\text{m}$, in the opposite direction of the walk-off in the third-harmonic crystal. In this way, the ir beam sweeps through the green beam as both beams traverse the third-harmonic crystal, providing maximum overlap of the ir and green beams in the crystal, and maximum uv generation. The use of the smaller walk-off-compensating crystal increases the third-harmonic generation by 50% compared to the best that could be obtained without it, and results in total conversion of the green to uv along a horizontal line through the center of the beam in the far field. The uv beam is near diffraction limited, with weak Maker fringes visible in the far-field pattern, in the vertical direction. The total ir to uv conversion in this system, at a pulse repetition rate of 500 Hz, is 25%, resulting in $112\text{-}\mu\text{J}$ pulses at 355 nm. Relative to the light incident on the BBO, the conversion efficiency, at 500 Hz, is 32%.

The entire 355-nm laser system was built using techniques and material systems that have been tested over a temperature range of -40 to 71°C , under shocks in excess of 20 G, and with the vibrations encountered in demanding flight scenarios [1].

Figure 1-2 shows a photograph of the optical head of the 355-nm laser system. It fits in an envelope that is 20 cm long by 7 cm wide by 4 cm deep, and occupies a volume of <0.5 liters.

The system was characterized at pulse repetition rates between 100 and 500 Hz. The ir, green, and uv output of the system are shown as a function of repetition rate in Figure 1-3. (As a result of the numerous optical surfaces in the system, the total of the outputs at the three wavelengths is less than the energy exiting the amplifier.) The slightly lower conversion efficiency from the ir at lower repetition rates is balanced by increased ir pulse energies, resulting in uv pulse energies that are nearly independent of the pulse rate. The 355-nm output pulse has a nearly top-hat temporal profile, with a 700-ps full width at half-maximum and detector-limited 200-ps rise and fall times, as shown in Figure 1-4. It shows clear signs of saturation.

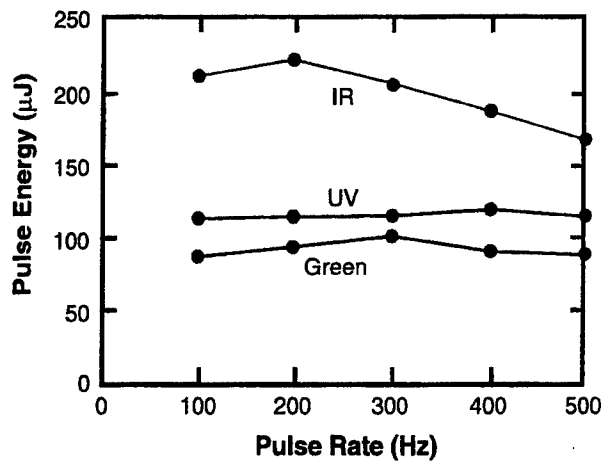


Figure 1-3. Output energy of laser head in the ir, green, and uv as a function of repetition rate.

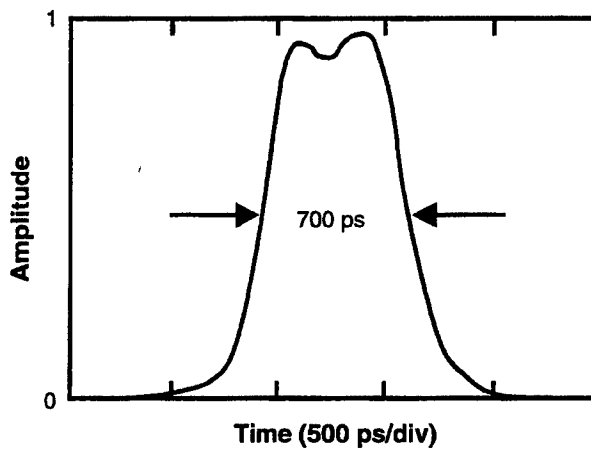


Figure 1-4. Temporal profile of 355-nm pulse.

In conclusion, a 355-nm laser system was constructed and characterized. The system produces $>100 \mu\text{J}$ of 355-nm radiation at pulse rates up to 500 kHz, in a diode-pumped optical head that occupies a volume of <0.5 liters. This turnkey system was designed to survive the demands of military use, industrial use, and flight. While this system was built for a MALDI (matrix-assisted laser desorption and ionization) application, the availability of such compact, fieldable tools should open up several application areas.

J. J. Zayhowski
A. L. Wilson, Jr.

REFERENCES

1. J. J. Zayhowski and A. L. Wilson, Jr., *IEEE J. Quantum Electron.* **38**, 1449 (2002).
2. J. J. Zayhowski and C. Dill III, *Opt. Lett.* **19**, 1427 (1994).
3. J. J. Zayhowski, *Laser Focus World* **35** (August), 129 (1999).
4. J. J. Zayhowski, C. Dill III, C. Cook, and J. L. Dancu, *OSA Trends in Optics and Photonics*, Vol. 26, *Advanced Solid-State Lasers*, M. M. Feyer, H. Injeyan, and U. Keller, eds. (Optical Society of America, Washington, D.C., 1999), p. 178.
5. J. J. Zayhowski, *Rev. Laser Eng.* **26**, 841 (1998).
6. T. S. Rose, M. S. Hopkins, and R. A. Fields, *IEEE J. Quantum Electron.* **31**, 1593 (1995).
7. U. Roth, M. Tröbs, T. Graf, J. E. Balmer, and H. P. Weber, *Appl. Opt.* **41**, 464 (2002).

2. ELECTRO-OPTICAL MATERIALS AND DEVICES

2.1 SILICON MICROLENS FABRICATION BY MESA ETCHING AND MASS-TRANSPORT SMOOTHING

The fabrication of Si microlenses by mesa etching and mass-transport smoothing, similar to those previously developed for III-V compounds [1],[2], has been demonstrated for the first time. Silicon microlenses are desirable for microoptical applications, especially for Si optical benches and microelectromechanical systems.

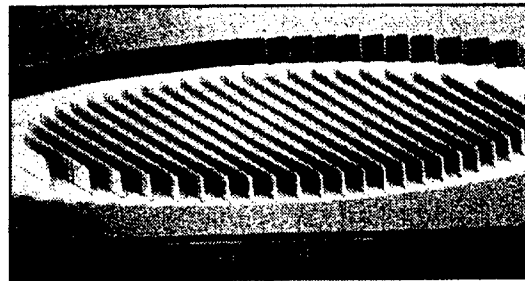
As widely demonstrated in III-V compounds, surface energy and surface atomic mobility give rise to mass transport in etched structures during heat treatment. The basic principles are expected to be applicable to Si. In practice, however, the relatively low vapor pressure [3] and strong surface oxidation can become considerable obstacles in achieving Si mass transport. Recently, Sato et al. [4] have demonstrated Si mass transport at 1100°C in micrometer-sized structures. To make practical microlenses of several-hundred-micrometer apertures requires complete mass-transport smoothing of mesa structures of tens of micrometers dimensions.

Figure 2-1(a) shows a scanning electron micrograph of a multi-mesa preform etched in a Si wafer. It was formed by using photolithography and reactive ion etching. Within each preform, the mesas have a constant height (11.0 μm in the present sample) but with a width distribution designed for the desired lens profile. The etched wafer was diced (cleaved) into ~2-cm size and cleaned in solvents. It was then HF-soaked and subsequently RCA ($\text{H}_2\text{O}:\text{NH}_4\text{OH}:\text{H}_2\text{O}_2 = 5:1:1$) cleaned. The wafer was then rinsed in de-ionized water, blown dry, and placed facing down on a quartz plate in which a slot of several hundred micrometer depth had been milled out in the central region. The outer region of the wafer rests on the planar surface (unmilled region) of the quartz plate and serves as a vapor protection for the central region, against thermal etching in the heat treatment.

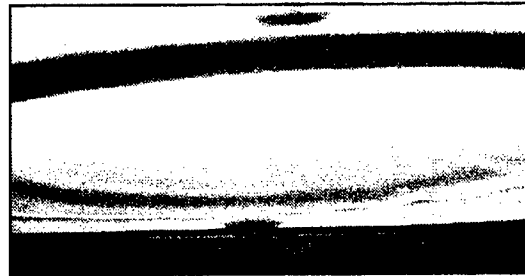
The heat treatment was carried out in a quartz furnace tube in which was flowed a mixture of H_2 and Ar gases. (Pure Ar was used in some experiments.) The furnace was heated to 1250°C for typically 80 h.

Figure 2-1(b) shows a scanning electron micrograph of a smoothed microlens after the heat treatment. Figure 2-2(a) shows an optical micrograph of the top view of a similar microlens. A stylus surface-profiling trace is shown in Figure 2-3, in which an accurate spherical profile of a radius of curvature of 1244 μm is observed except for an outer region of ~10- μm width. The effective aperture of the microlens as estimated from Figure 2-3 is 200 μm . The good lens quality is also reflected in the sharp image in Figure 2-2(b), formed by the microlens, of a partially closed iris in the microscope [1].

The present results are generally analogous to those previously observed in III-V compounds and can be understood in terms of the same basic mechanisms of surface energy and surface atomic mobility [2]. However, the mass-transport rate estimated from the existing vapor pressure data of Si [3] would

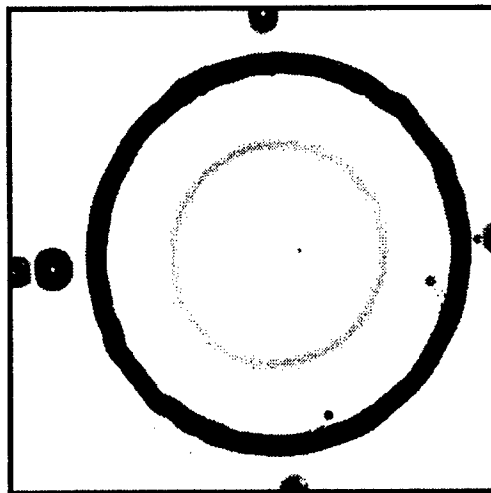


(a)

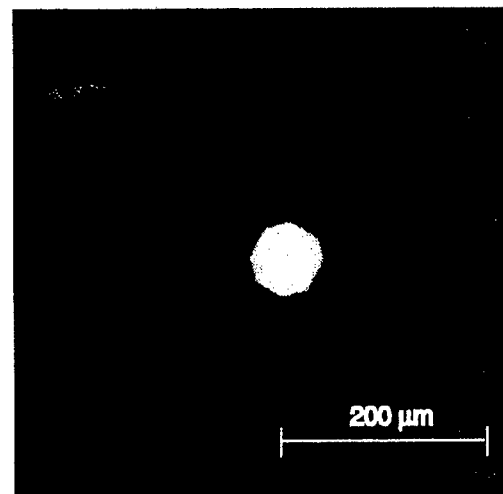


(b)

Figure 2-1. Scanning electron micrograph of Si microlens fabrication: (a) etched multi-mesa preform and (b) microlens formed after mass-transport smoothing.



(a)



(b)

Figure 2-2. Optical micrographs of (a) top view of mass-transported Si microlens and (b) image formed by microlens surface of the partially closed iris in the microscope. Note that the large ring of dark band in (a) is the graded sidewall of the etched well inside which the microlens is located.

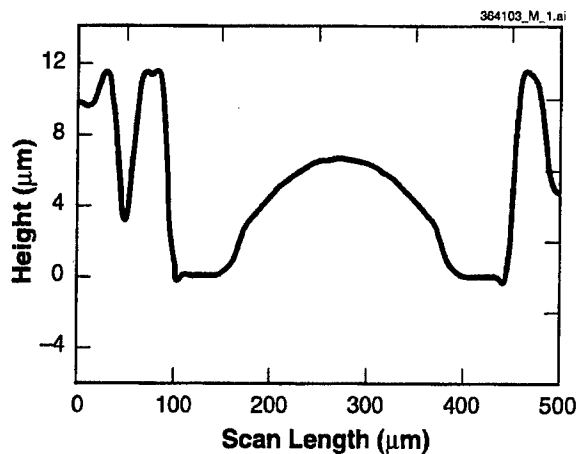


Figure 2-3. Stylus surface-profiling trace of Si microlens [cf. Figure 2-2(a)].

predict a process time some 2 orders of magnitude longer than presently observed. It appears that surface dissociation might have been greatly enhanced in this vapor environment.

The surface oxide formed after the RCA cleaning appeared to be volatile and did not impede mass transport. Care was exercised in this work in preventing further oxidation during the process. Additional care was needed in surface treatment and in wafer protection for mass transport for high yield of good microlenses.

In conclusion, surface energy and mass transport have been used for microlens fabrication in Si for the first time. The process is relatively simple and precisely controlled. The microlenses are promising for practical microoptical applications.

Z. L. Liao M. B. Stern*
D. C. Flanders*

*Author not at Lincoln Laboratory.

REFERENCES

1. Z. L. Liao, D. E. Mull, C. L. Dennis, R. C. Williamson, and R. G. Waarts, *Appl. Phys. Lett.* **64**, 1484 (1994).
2. Z. L. Liao, *Mater. Chem. Phys.* **46**, 265 (1996).
3. D. E. Gray, ed., *American Institute of Physics Handbook*, 3rd ed. (McGraw-Hill, New York, 1972), p. 300.
4. T. Sato, I. Mizushima, J. Iba, M. Kito, Y. Takegawa, A. Sudo, and Y. Tsunashima, *1998 Symposium on VLSI Technology: Digest of Technical Papers* (IEEE, Piscataway, N.J., 1998), p. 206.

3. SUBMICROMETER TECHNOLOGY

3.1 PROSPECTS FOR PHOTOLITHOGRAPHY AT 121 nm

One of the obvious ways to enhance the resolution of optical lithography is to reduce the exposure wavelength. Indeed, photolithography has gradually evolved from using the visible emission of mercury discharge lamps (g-line, 436 nm) to the near-uv emission of mercury lamps (i-line, 365 nm), to the so-called deep-uv emission of KrF excimer lasers (248 nm), and recently to the even deeper-uv emission of the ArF excimer lasers (193 nm). It is widely anticipated that within a few years leading-edge lithography will be performed at the vacuum-uv wavelength of the F₂ excimer lasers (157 nm). At that point, the printed dimensions will be in the range 50–70 nm, i.e., less than half of the wavelength. In light of this progression, it is natural to explore further options to reduce the lithographic wavelength, and thereby possibly enable the patterning of dimensions of 35–50 nm. The most promising candidate is the 121.6-nm emission of atomic hydrogen, widely familiar to astronomers and atomic physicists as the Lyman- α line. This wavelength has several potential advantages over other candidates: it is short enough to afford a meaningful advantage in resolution when transitioning from 157 nm, and the 121-nm line can be spectrally narrow, holding out the hope for the design of catadioptric optical systems with negligible chromatic aberrations. This is in contrast with another possible wavelength, the Ar₂ emission at 126 nm, which is several nanometers broad.

The development of a new lithographic technology requires careful evaluation of a large number of interlocking components. These include powerful radiation sources, whether lasers or lamps; constraints on the optical design as determined by linewidth, availability of transparent optical materials, and effective optical coatings; ambient considerations; photoresists with comfortable latitudes in terms of plasma etch resistance, resolution, and line edge roughness; and practical photomask technology [1]. In this report we focus on sources, photoresist, and an experimental demonstration of 121-nm lithography.

For the experiments described here, we primarily used a photomultiplier tube (PMT) with a RbTe solar-blind photocathode (response 110–360 nm). The PMT was typically operated at bias voltages between –800 and –900 V. The absolute response of this detector at 121 nm was determined by cross calibration with a NIST-certified Si photodiode. Since the Si photodiode has a high detection sensitivity in the visible, a 121-nm bandpass filter was used to reject visible wavelengths. This filter transmitted 20% of 121-nm light and <0.1% of radiation above 250 nm. Using the diode cross-calibration technique, we determined the sensitivity of our PMT to be 2 mA/W at a bias voltage of –850 V.

For most of the work described here, we used a high-pressure dc-discharge lamp built by Professor Murnick's group at Rutgers University. The lamp generates hydrogen Lyman- α radiation via resonant energy transfer from neon excimer molecules to molecular hydrogen, which leads to dissociation and excitation [2]. This lamp operates at near atmospheric pressures and utilizes 0.01% H₂ in Ne. The lamp output spectrum in the vacuum-uv and uv regions shows only the 121-nm line, seen in Figure 3-1. Since

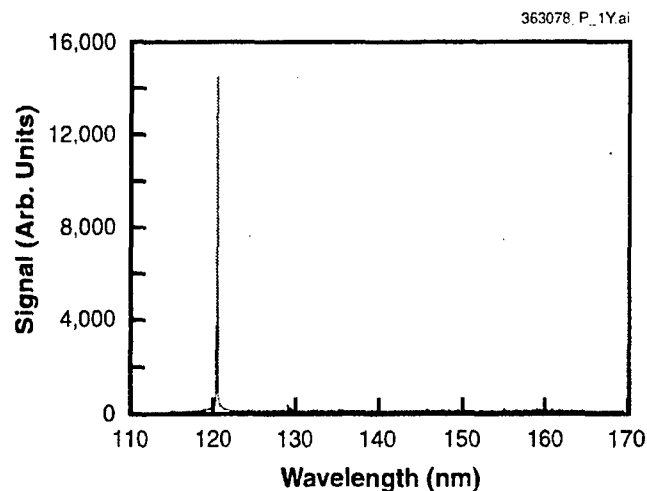


Figure 3-1. Spectral output of hydrogen Lyman- α discharge lamp built by T. McCarthy and D. E. Murnick of Rutgers University.

the emission is an atomic transition, the linewidth is expected to be extremely narrow. Previous characterization of the linewidth of this discharge was limited by instrumental resolution to an upper bound of 0.01 nm [2]. Total discharge power into 4π sterad is ~ 10 mW, and the size of the discharge is estimated to be $< 1 \text{ mm}^3$.

The dc-discharge configuration described above is very useful for metrology and initial lithography experiments, but it is limited in its scalability to a higher power. Therefore, we explored an alternative means to generate 121.6-nm radiation, one that may be scalable to at least several watts of usable power, in collaboration with Science Research Laboratory (SRL) of Somerville, Massachusetts. We tested the feasibility of generating Lyman- α radiation in a dense focused plasma configuration, which had been optimized for extreme ultraviolet (EUV) application. The focused plasma is needle shaped, ~ 0.25 mm in diameter, and 1.7 mm long. In our experiments the EUV GEN-III source built by SRL was filled with 0.08–0.8-Torr H_2 and operated in a single shot mode. The emitted energy was detected and measured with the PMT described above. The spectrum of this emission was not fully analyzed, but rather it was bracketed by the high-energy cutoffs of the PMT (110 nm) and of a CaF_2 blank (122 nm). The total light emitted into this 110–122-nm band, assumed to be primarily Lyman- α radiation, was found to be 6% of the stored capacitor energy, or 0.5 J per pulse. By comparison, the efficiency of generating 13-nm EUV radiation with the same source is an order of magnitude lower. The repetition rate of the focused plasma source is potentially scalable to > 1 kHz, so that we anticipate that ~ 1 -kW average 121-nm power can be obtained in such a system [3].

When a new wavelength is considered for lithography, the feasibility of developing suitable photoresists looms high on the agenda. Typically the driving force is the high absorption at the new

wavelength of the polymer used at the previous wavelengths; aromatics are too absorptive at 193 nm, and hydrocarbon-based polymers are too absorptive at 157 nm. Thus, the issue of a suitable resist platform at 121 nm must be addressed in any study of this technology. Two questions must be answered. First, what is the optimal thickness of resists developed for longer wavelengths, i.e., what is their absorption coefficient at 121 nm. Second, what is their photochemical response, i.e., do they still act as resists with reasonable dose and contrast.

We have set out to measure the 121-nm absorbance of a number of polymers and photoresists, since in this spectral range almost no information is available in the literature. In our measurements, three thicknesses for each material of interest were spin cast onto 2-mm-thick MgF_2 substrates and baked as needed. The film thicknesses were determined with ellipsometry in separate experiments where the substrates were silicon wafers. The 121-nm transmission of the coated MgF_2 substrates was measured directly with our hydrogen discharge lamp and the solar-blind PMT described above, and normalized to the transmission of the uncoated substrates. The film absorbance was plotted vs sample thickness, and the absorption coefficient was extracted from the slope of the linear fit to the data. In this manner we have determined the absorbance of a number of polymers that would be candidates as photoresist constituents and of four commercial photoresists formulated for higher-wavelength applications (157–248 nm). The results are tabulated in Table 3-1, including the film thickness if its optical density were to be kept at the conventional value of 0.4.

The main observation from these data is that all materials, i.e., hydrocarbon-, fluorocarbon-, and silicon-containing, have 121-nm absorption coefficients of at least $5 \mu\text{m}^{-1}$, and in most instances closer to $20 \mu\text{m}^{-1}$. These values imply that photoresists at 121 nm must be very thin, around 20–40 nm, much thinner than even hydrocarbon-based resists at 157 nm. At present, we are not aware of any chemical platforms that would reduce these absorption coefficients. Therefore, a practical implementation of 121-nm lithography will have to deal with the preparation of such ultrathin films and with the development of bilayer resists or reliable surface-imaging processes.

In order to answer our second question, we have performed large-spot exposures of photoresist materials listed in Table 3-1 at thicknesses of 18–20 nm. In these experiments, Si wafers coated with photoresists were exposed to 121-nm light through a 6-mm aperture. Exposure was followed by a 90-s, 130°C post-exposure bake and 20-s development in a commercial 0.26-N aqueous base developer. The remaining thickness of photoresist was measured with an ellipsometer. Normalized thickness remaining (NTR) is plotted vs incident 121-nm dose in Figure 3-2. All the photoresists exhibited low E_0 (incident dose to clear), usually less than $1 \text{ mJ}/\text{cm}^2$. These values are in agreement with the high absorption coefficient. A comparison to the respective E_0 at 157 nm shows that for any given resist the E_0 scales approximately inversely with the absorption coefficient, so that the absorbed dose per unit volume is constant. The resists also exhibited very high contrast. In fact, measurement of the steepness of the NTR slope with dose was limited by the ellipsometer accuracy. As can be seen from the curve of resist A, at higher incident doses the resists can also exhibit negative-tone behavior. Such behavior was observed for all the resists tested, in rough agreement with similar behavior observed at 157 nm. This behavior has been attributed [4] to photo-induced crosslinking of the polymer itself, with little contribution from the

TABLE 3-1

121-nm Absorption Coefficients and Maximum Thickness for Optical Density 0.4 of Several Polymers Relevant to Photoresist Process and of Several Commercial Resists Used for Higher-Wavelength Lithography

Compound*	Absorption Coefficient (μm^{-1} , Base 10)	Thickness for Optical Density 0.4 (nm)
Polymers		
Nafion	5.7	70
P(HFIP-Styrene)	10	40
HSQ Spin-on-Glass	12	33
PMMA	19	21
p(TBA)	17	24
PHOST	26	15
Long-Wavelength Photoresists		
A	22	18
B	24	17
C	25	16
D	30	13
*HFIP = hexafluoroisopropyl; HSQ = hydrogen silsesquioxane; PMMA = poly(methyl methacrylate); p(TBA) = poly(t-butyl acrylate); PHOST = poly(hydroxystyrene).		

photogenerated acid. Given the high photon energy, such a photo-physical reaction is not surprising. The onset of the negative dose varied from 1.4 mJ/cm² for resist A to 38 mJ/cm² for resist B. In summary, it appears that the photochemical response of resists at 121 nm is similar to that at 157 nm, and no unusual effects are observed that could be attributed to the higher photon energy.

To date, we have not constructed a 121-nm optical projection system, mainly because of the difficulties involving high-transmission LiF optics. Instead, we have demonstrated high-resolution printing by employing near-field photolithography with a phase shifting mask, in a manner similar to the technique

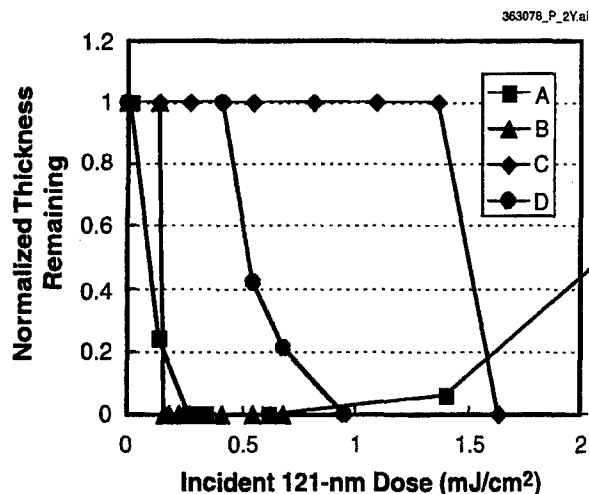


Figure 3-2. Normalized thickness remaining vs incident 121-nm dose for four commercial resists.

described in [5] for near-uv contact lithography. In our experiments a transparent MgF_2 substrate was patterned and etched to form steps whose height corresponds to a 180-degree phase shift. The height is given by $\lambda/[2(n-1)]$, which is 99 nm for the 121.6-nm wavelength and for a refractive index $n = 1.61$ of MgF_2 . When this mask is placed in contact with a resist-coated wafer, destructive interference takes place at the edge of the step, resulting in unexposed resist. This method is the near-field equivalent of chromeless projection phase shifting lithography, and it has been shown to enable printing of features of dimensions approximately one third of the wavelength [5]. For 121 nm one would therefore expect a resolution of ~ 40 nm.

The steps in the MgF_2 were formed by patterning gratings in photoresist using i-line contact lithography. First, a master mask in fused silica, having $2\text{-}\mu\text{m}$ chromium lines and spaces, was duplicated into photoresist on a 0.2-mm-thick fused-silica flex mask. The flex mask was then contacted to the MgF_2 substrate, which had been precoated with $0.5\ \mu\text{m}$ of commercial i-line resist. Following resist exposure and development, the MgF_2 sample was etched by argon ion milling. Argon ions at 500-V energy, 100-mA current with 0.5-mA/cm^2 current density were used. The ion miller is equipped with a neutralization source for reducing space-charge effects. The material removal rates were 19 nm/min for the photoresist and 38 nm/min for the MgF_2 . After timed etching, the remainder of the photoresist was stripped, and the depth of the etched features in MgF_2 was found to be within 10% of the nominal value of 99 nm. No increase in surface roughness was noticeable at the bottom of the etched trenches.

For printing phase edges at 121 nm with this mask, 20 nm of photoresist A described above were spin cast onto a silicon wafer. Intimate contact between the wafer and the MgF_2 mask was essential for

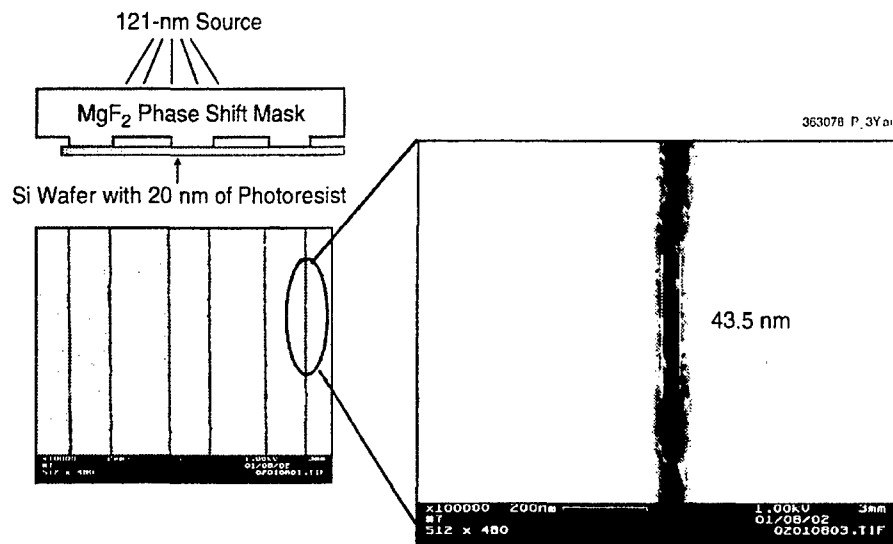


Figure 3-3. Schematic of near-field contact mode photolithography with phase shift mask (upper left) and scanning electron micrographs of the 43-nm phase edges printed with such a mask.

obtaining high contrast in the resist. To achieve it, we used a custom-built wafer holder with multiple set screws, which compressed the back of the wafer over an approximately half inch square area. Best exposure results were obtained for incident doses between 2 and 3 times E_0 , i.e., between 0.6 and 1 mJ/cm² of 121-nm radiation. With this process, lines 43 nm wide, corresponding to $\approx \lambda/3$, were obtained, as shown in Figure 3-3. The linewidth did not change appreciably over the dose range from 0.6 to 1 mJ/cm². Remarkably, even though the initial resist was very thin, atomic force microscopy revealed practically no unexposed thickness loss, as seen in Figure 3-4, in agreement with the contrast curve of Figure 3-2. These results indicate that we were able to realize the expected advantage in resolution afforded by the short wavelength of 121 nm.

V. Liberman M. Rothschild
P. G. Murphy S. T. Palmacci

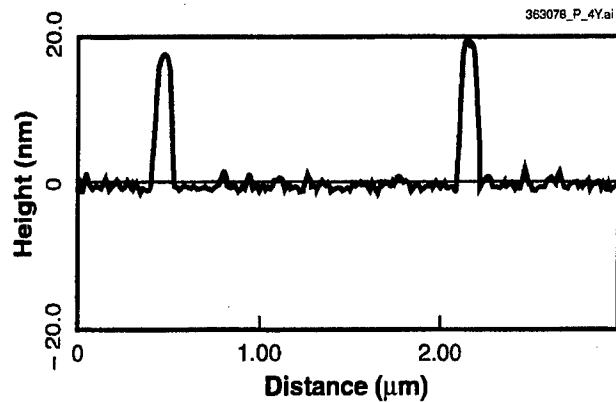


Figure 3-4. Atomic force microscopy cross section of the photoresist lines, printed as shown in Figure 3-3.

REFERENCES

1. V. Liberman, M. Rothschild, P. G. Murphy, and S. T. Palmacci, to be published in *J. Vac. Sci. Technol. B*, Nov.-Dec. 2002.
2. J. Wieser, M. Salvermoser, L. H. Shaw, A. Ulrich, D. E. Murnick, and H. Dahi, *J. Phys. B* **31**, 4589 (1998).
3. A. Bykanov, private communication.
4. T. H. Fedynyshyn, R. R. Kunz, S. P. Doran, R. B. Goodman, M. L. Lind, and J. E. Curtin, *Proc. SPIE* **3999**, 335 (2000).
5. J. A. Rogers, K. E. Paul, R. J. Jackman, and G. M. Whitesides, *J. Vac. Sci. Technol. B* **16**, 59 (1998).

**This Page Intentionally
Left Blank**

4. BIOSENSOR AND MOLECULAR TECHNOLOGIES

4.1 EEL HIGH-ENERGY BIOFUEL CELL

Biologically based fuel cells with very high energy densities are being developed. As shown in Figure 4-1, our approach is to genetically engineer bacteria to pump electric current in one direction, and then cause the bacteria to self-assemble in series and parallel in an array to produce useful amounts of voltage and current. This approach, termed EEL (Engineered Electrocyte Layers) since it mimics how electric eels produce electricity, should result in biofuel cells with energy densities up to 60× greater than conventional batteries. These biofuel cells should be inexpensive to produce because the bacteria reproduce themselves, and furthermore they should be inexpensive to refuel since the bacteria can metabolize fats, sugars, waste food, or almost any other form of organic matter. Potential applications for such refuelable, high-energy-density power sources include powering mobile electronic devices, long-lived deployable sensors, soldiers' field gear, and electric vehicles. In small-scale experiments funded by the Lincoln Laboratory New Technology Initiatives Program (NTIP), we have demonstrated some of the key principles of this approach, including engineering suitable bacteria and maintaining the bacteria under typical biofuel cell conditions for over two months.

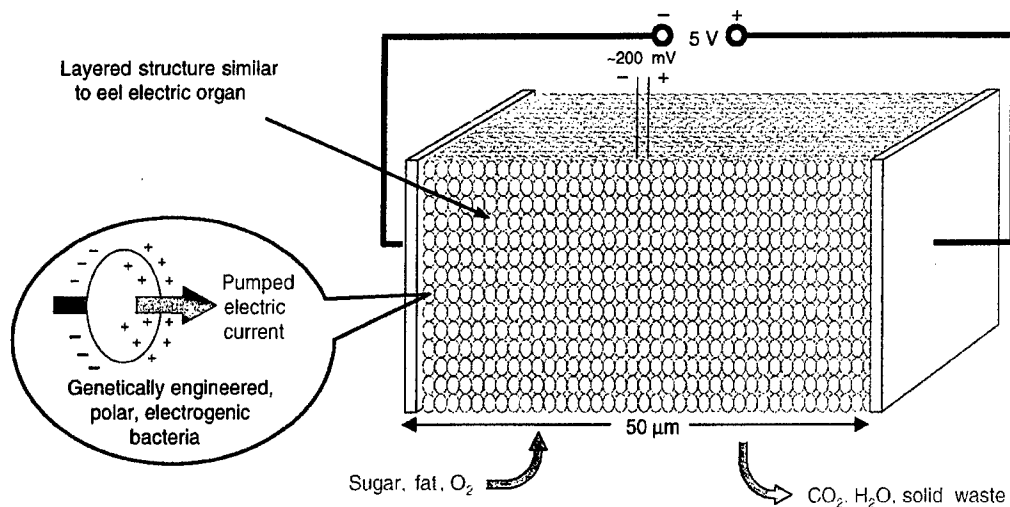


Figure 4-1. EEL (Engineered Electrocyte Layers) biofuel cell. It should have high energy density, approximately 60× greater than batteries, and should be inexpensive to produce and refuel.

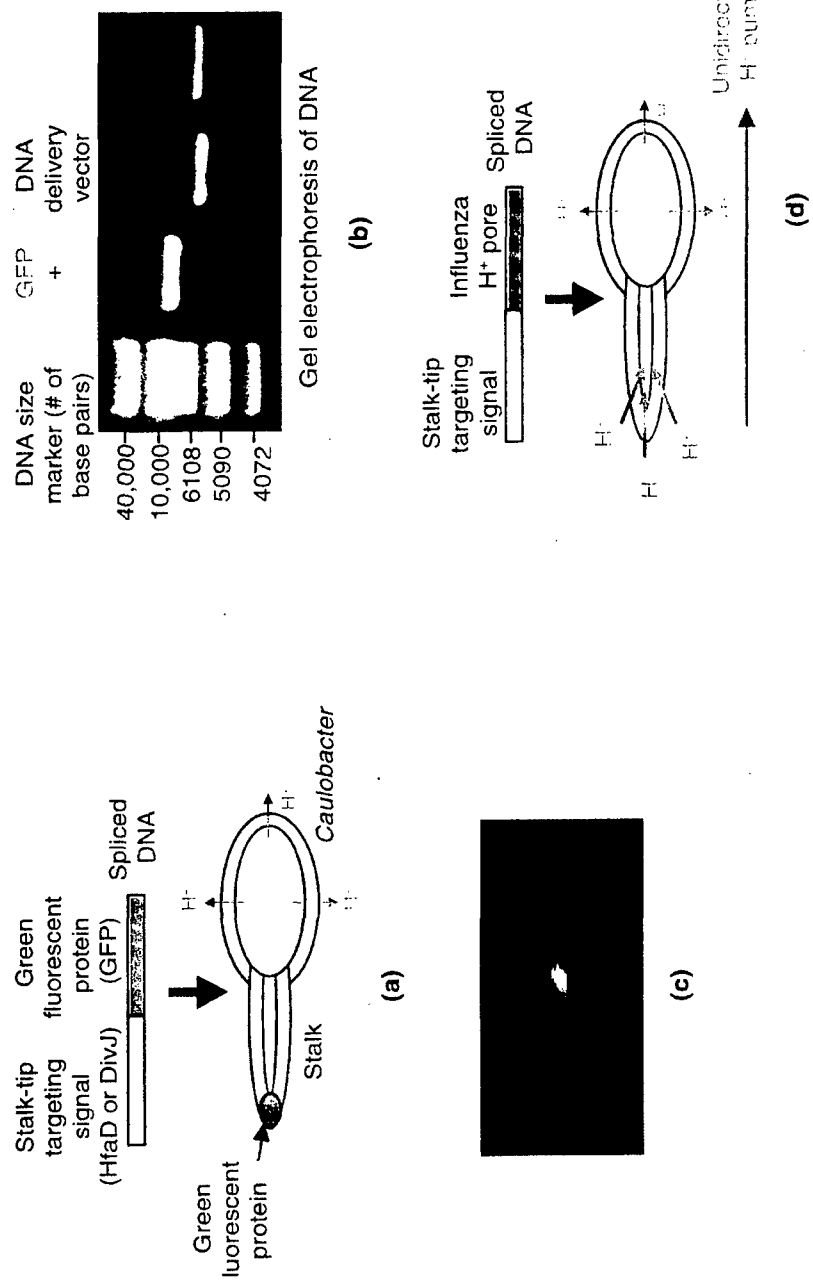


Figure 4-2. Genetic engineering of *Caulobacter*: (a) Test of protein targeting, (b) spliced genes, (c) *Caulobacter* with HfaD-GFP, as viewed with 400x fluorescent microscope (targeting still being optimized), and (d) adding stalk-tip proton pore.

Caulobacter crescentus bacteria [1] are used because they are already naturally asymmetric with a stalk on one end [2] and only have proton transport in the main body, not the stalk [3],[4]. The bacteria also have holdfast adhesion molecules on the tip of the stalk [5], permitting them to be attached and oriented all in the same direction in a biofuel cell. We have previously shown that low-phosphate growth medium can be used to lengthen the stalk and accent the asymmetry, and that dicyclohexylcarbodiimide (DCCD) or other chemicals can inhibit proton influx in the main body, only allowing protons to be pumped out there.

Since protons are actively pumped out of the main body, the bacteria will become electrically polarized if an engineered proton-permeable pore is targeted to the stalk at the other end. To test our ability to target proteins to the stalk, we have spliced natural stalk-tip targeting signals (HfaD, DivJ, and other signals) to green fluorescent protein (GFP), as shown in Figures 4-2(a) and 4-2(b). These genes have been transformed into *Caulobacter* bacteria, which then produce the corresponding proteins. Using a fluorescent microscope, we can determine the spatial location of the targeted GFP within individual bacteria, seen in Figure 4-2(c), and choose the best targeting signal for our purpose. As illustrated in Figure 4-2(d), the next step is to splice the best targeting signal to a proton-permeable pore from the influenza virus [6] in order to complete the engineering of the EEL bacteria. Protons will then passively diffuse into the stalk end of the bacteria and be actively pumped out of the other end, producing the desired ion flow.

As shown in Figure 4-3, we have demonstrated the maintenance of *Caulobacter* bacteria under typical biofuel cell conditions for periods of over two months. On both glass and plastic surfaces, the bacteria form self-organized, tightly packed monolayers, seen in Figure 4-3(a). Because all of the bacteria attach to the surface by the tips of their stalks, they are all pointed in the same direction and thus should all pump electric current in the same direction once the genetic engineering has been completed. The bacteria remain very firmly attached to the surfaces even after vigorous shaking. Because of the tight packing of the bacteria in the monolayer, ion leakage between bacteria should be minimal, although sealants can be added if necessary.

To prevent the bacteria in a biofuel cell from overgrowing, chemical growth inhibitors can be added to the medium. To demonstrate this, we tested various concentrations of sodium azide (NaN_3), aurovertin, and other growth inhibitors. Figure 4-3(b) shows that with the proper concentration of growth inhibitors, the number of bacteria can be held constant, with the bacteria neither dying out nor multiplying excessively. *Caulobacter* bacteria have been maintained in this state for periods of over two months. If the growth inhibitors are removed, the bacteria immediately begin to multiply, proving that they are indeed still alive.

To summarize, we are developing the EEL biofuel cell, a novel approach that uses genetically engineered bacteria to mimic the way electric eels produce electricity. These biofuel cells should have an energy density up to 60 \times greater than present batteries and could be refueled using waste food or almost any other organic matter. To prove the feasibility of this approach, we have demonstrated critical steps in engineering the bacteria, and we have shown that the bacteria can be maintained under typical biofuel cell conditions for over two months. In future experiments, we plan to measure the voltage difference and current flow across a monolayer of engineered bacteria.

T. H. Rider

T. L. Schmidt

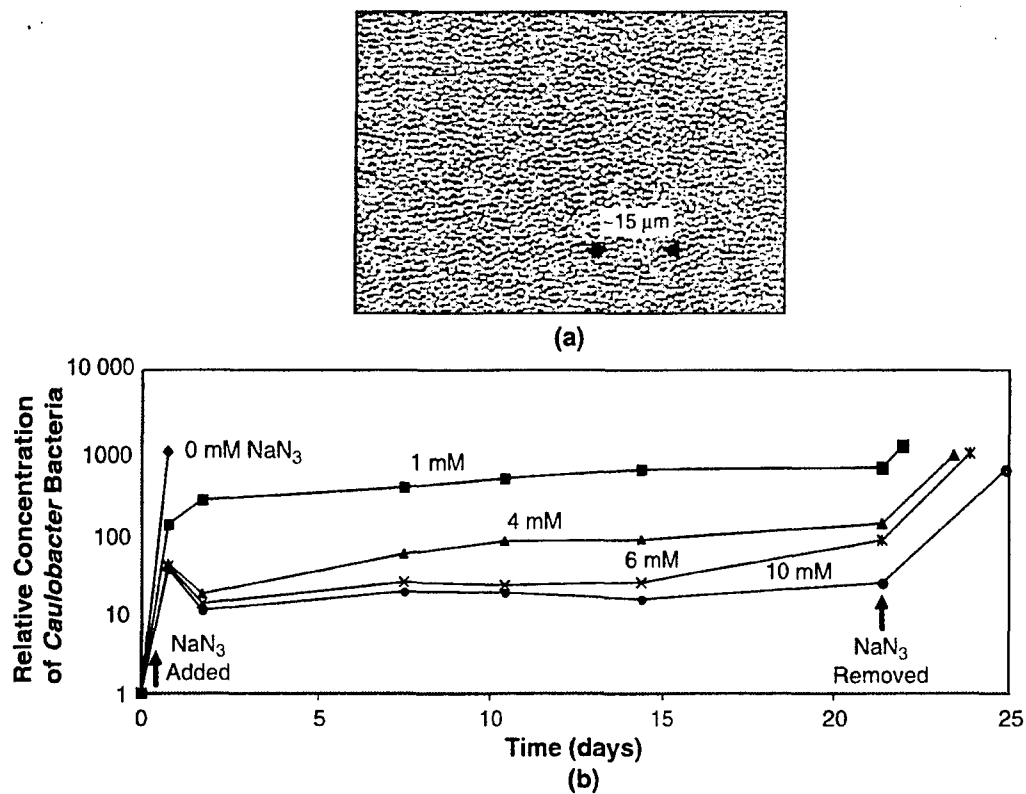


Figure 4-3. Maintenance of *Caulobacter* bacteria under typical biofuel cell conditions. (a) Bottom view of monolayer with 400 \times phase-contrast microscope, demonstrating that bacteria self-assemble into tightly packed monolayer. (b) Demonstration of constant number of live bacteria using NaN_3 or other growth inhibitors: growth when inhibitor is removed shows that bacteria are still alive.

REFERENCES

1. J. S. Poindexter, *Microbiol. Rev.* **45**, 123 (1981).
2. R. T. Wheeler, J. W. Gober, and L. Shapiro, *Curr. Opin. Microbiol.* **1**, 636 (1998).
3. K. M. Charrey and H. D. Kurtz, Jr., *Biotechnic Histochem.* **73**, 255 (1998).
4. S. Koyasu, A. Fukuda, Y. Okada, and J. S. Poindexter, *J. Gen. Microbiol.* **129**, 2789 (1983).
5. R. S. Janakiraman and Y. V. Brun, *J. Bacteriol.* **181**, 1118 (1999).
6. K. C. Duff and R. H. Ashley, *Virology* **190**, 485 (1992).

5. ADVANCED IMAGING TECHNOLOGY

5.1 POINT-SPREAD RESPONSE OF A THICK, BACK-ILLUMINATED CCD IMAGER

For several years, large-area, back-illuminated imagers have been made for a consortium of observatories led by the University of Hawaii's Institute for Astronomy [1],[2]. Because of strong interest in high quantum efficiency in the near-ir, these devices have been fabricated on high-resistivity wafers so that they can be made thicker than conventional back-illuminated imagers while still being fully depleted for good point-spread response. This report describes measurements of the optical point-spread response of these imagers in the blue and near-ir portions of the spectrum.

The point-spread response, also known as the intrapixel response, is the response of an image sensor to an optical spot which is raster scanned over an array of pixels. The optical spot must naturally be much smaller than the pixel size in order to accurately record the detailed response. We have described the system for performing this measurement [3], and it is illustrated schematically in Figure 5-1. An optical fiber is illuminated at one end by a light source, while the other (output) end is placed at the image plane of a photometric eyepiece. The tip of the fiber is re-imaged onto the device using a 50 \times refractive microscope objective and produces a spot about 3 μm in diameter. Note that the refractive objective has replaced a reflective objective reported in the earlier work and gives a somewhat smaller spot. The measurement consists of recording the output of a given pixel as the light spot is scanned over a small array of pixels surrounding the pixel under study. In this way we obtain a map of the response that reveals the degree of optical crosstalk into adjacent pixels as well as information on how the pixel structure influences the response.

The devices used for this study were three-phase charge-coupled devices (CCDs) with 15- μm pixels made with a triple-polysilicon, buried-channel process on 5000 $\Omega\cdot\text{cm}$ p -type silicon. The wafers are

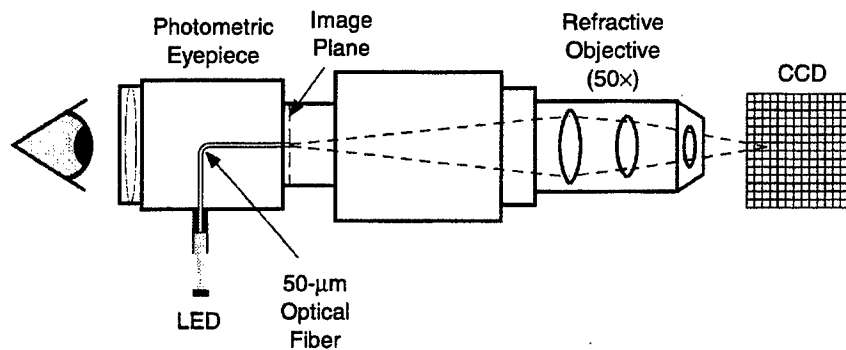
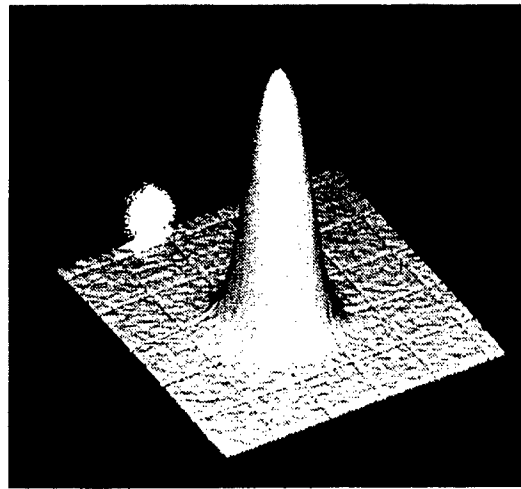
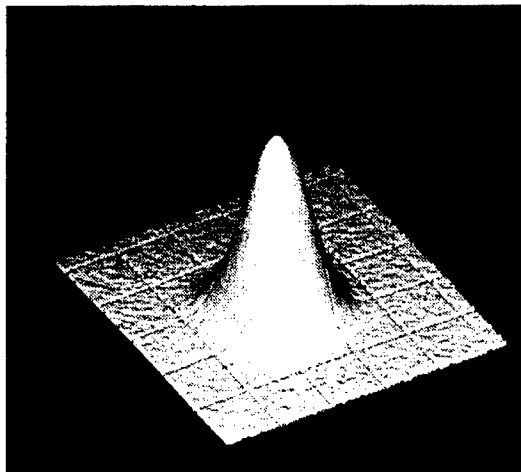


Figure 5-1. Illustration of system for measuring the point-spread response of an image sensor to a light spot.



(a)



(b)

Figure 5-2. Surface plots of optical response of pixel to 430-nm light spot scanned over a $80 \times 80\text{-}\mu\text{m}$ subarray made (a) with two of the clock voltages at +4 V and the third at -6, and (b) with one phase at +0 V and two at -8 V. A grid depicting the pixel boundaries has been superimposed on the data.

chemically thinned to about $40\text{--}50\ \mu\text{m}$, and a thin p^+ layer is grown on the back surface using molecular beam epitaxy. An antireflection coating is deposited as the final step. Because the device thickness is much greater than the pixel dimensions, it is important that the device be fully depleted and have sufficiently strong fields to drive the photoelectrons into the CCD wells before significant lateral diffusion occurs. Without full depletion, photoelectrons that are generated in the nondepleted region near the back surface

will diffuse laterally before they reach the depletion layer edge, and a substantial portion of the carriers will ultimately be collected in several surrounding pixels.

Figure 5-2 illustrates surface plots of the response of a pixel in the center of an $80 \times 80\text{-}\mu\text{m}$ scanned region on a $43\text{-}\mu\text{m}$ -thick device. A grid representing the boundaries of the pixels has been superimposed on the data as a visual aid. At the wavelength of 430 nm used in this measurement, the optical absorption length in silicon is $<0.3\text{ }\mu\text{m}$. The photoelectrons are therefore generated close to the back surface, and this provides a sensitive test of full depletion and of the point-spread response. The scan in Figure 5-2(a) was taken with two of the three phases set to $+4\text{ V}$ and the third phase at -6 V , and that in Figure 5-2(b) was taken with one phase at 0 V and the two remaining phases at -8 V . The results in Figure 5-2(a) show a distribution of collected photoelectrons that falls rapidly as the spot moves into adjacent pixels and is consistent with full depletion. The results in Figure 5-2(b) show a somewhat broader distribution with more spillover into adjacent pixels. This is a result of the lower clock voltage which reduces the electric field across the bulk and indicates that the device is either marginally or not fully depleted.

Figure 5-3 shows results of one-dimensional scans through the center of the pixel both along and orthogonal to the channel direction for the conditions of Figure 5-2(a). The results show a smooth bell-shaped response that falls off as the spot is moved into adjacent pixels. Another measure of the crosstalk is how much signal falls in the surrounding pixels when the center of a given pixel is illuminated. For the case illustrated in Figures 5-2(a) and 5-3, the center pixel collected 84% of the charge. For the case

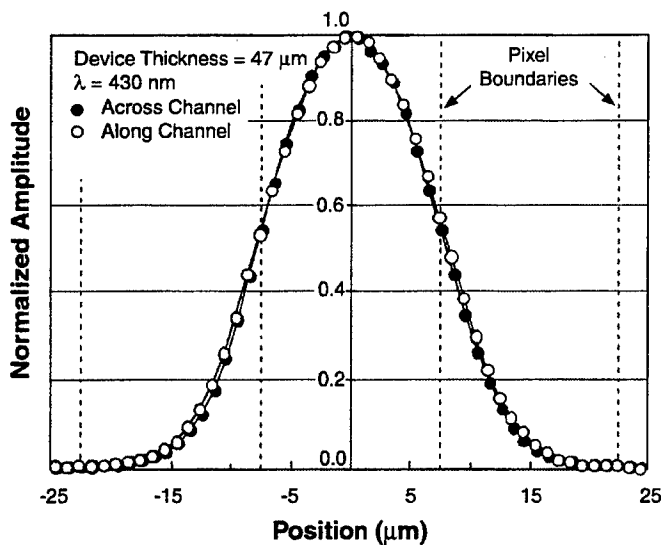


Figure 5-3. Optical response to light spot scanned through the center of the pixel along and across the direction of the channel.

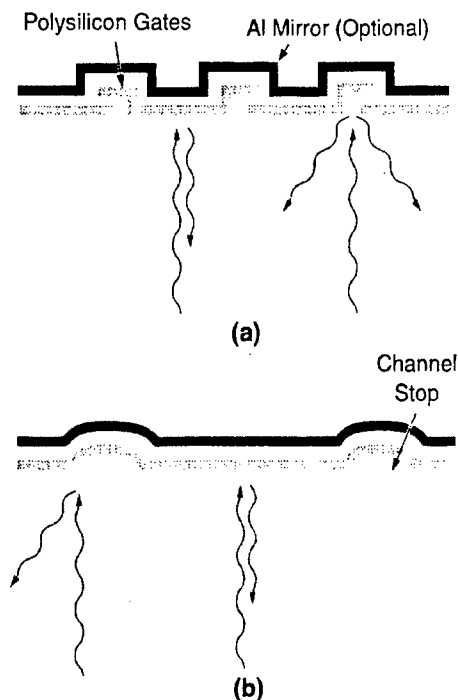
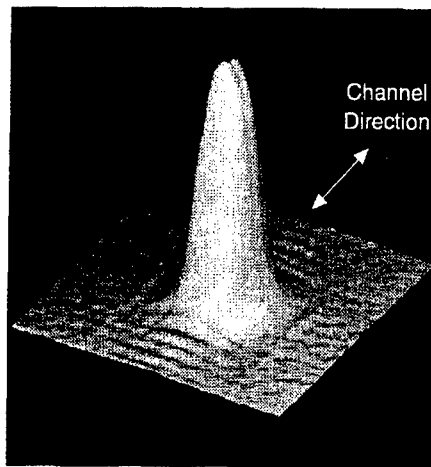


Figure 5-4. Depiction of scattering of near-ir light off surface features of a charge-coupled device (CCD). The illumination enters a back-illuminated device and is scattered (a) by the polysilicon-gates overlaps and (b) by the thick-oxide channel stops.

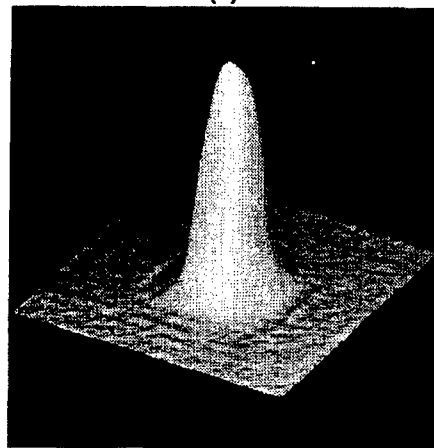
with the lower clock voltage settings that produced the scan of Figure 5-2(b), the center pixel collected 60% of the charge.

In the near-ir the penetration depth of the radiation is much greater, and accordingly the point-spread response will not be as sensitive to whether the device is fully depleted or not. We find that the overall response is indeed as tightly distributed as that of Figure 5-2(a) for the same voltage settings, but we have observed an additional mechanism for crosstalk that is described in Figure 5-4 and has not been heretofore explored. A significant portion of light at wavelengths beyond around 900 nm will penetrate through a CCD 40–50- μm thick and be partially reflected off the surface features of the device back into the silicon substrate. Most of this reflection is on axis, but a portion of it occurs at steeper angles than the incident radiation when the light encounters the sloping sides of the channel stops or the gaps in the polysilicon gate electrodes. Some of this scattered component reaches neighboring pixels and generates crosstalk.

Figure 5-5 shows surface plots of the photoelectron distribution taken with a light spot at 950 nm scanned over an 80 \times 80- μm field. The device in Figure 5-5(a) had an aluminum film deposited over the



(a)



(b)

Figure 5-5. Surface plots of pixel response at 950 nm on devices (a) with and (b) without an Al film deposited over the CCD gates.

gate structure, while the device in Figure 5-5(b) did not. The purpose of the film was to explore improvements in the near-ir quantum efficiency that result from more light being reflected back into the CCD. Apart from the main response, there are features in these plots that can be associated with the structural features in the device illustrated in Figure 5-4. For example, the ridges running parallel to the CCD channel are the result of reflections off the channel stops, while the reflections off the gate-overlap regions give rise to the closely spaced ridges perpendicular to the channel direction. In both cases the Al

film has enhanced these features by adding additional reflected light back into the CCD. In view of the enhanced crosstalk, as well as the fact that the quantum efficiency has been measured to be only marginally improved, we conclude it is not advisable to use this film.

B. E. Burke
T. A. Lind
M. J. Cooper

5.2 RADIATION EFFECTS ON AVALANCHE PHOTODIODES

Geiger-mode avalanche photodiodes (APDs), in practice, are operated by electronically arming them to a reverse bias voltage above their breakdown threshold. This is usually achieved by means of a diode switch, a resistor, or more conveniently, a *p*-type field-effect transistor (FET) switch [4], as shown in Figure 5-6. When armed, an avalanche can be triggered in the APD junction by either an optically or thermally generated electron-hole pair (EHP). To preclude inadvertent optical generation of an EHP, a light shield can be used to block light from reaching the APD; consequently, dark current will be the only source of EHP generation. A single avalanche event produced by a thermally generated EHP traversing the high-field region is referred to as a dark count. After an APD begins to avalanche, that avalanche may be quenched by lowering and maintaining the reverse bias voltage below the breakdown voltage of the device for some finite duration. Quenching can be achieved in practice by switching on an *n*-FET transistor with its drain connected to the APD cathode, as shown in the Figure 5-7.

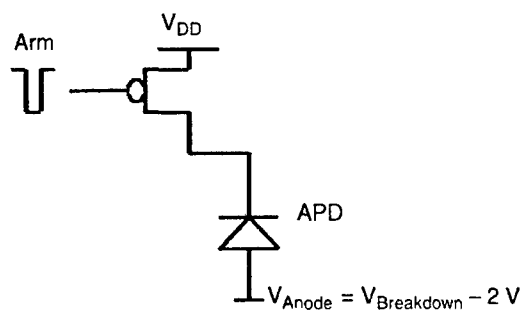


Figure 5-6. Operation of avalanche photodiode (APD) by arming to a reverse bias voltage above its breakdown threshold by means of a *p*-type field-effect transistor (FET).

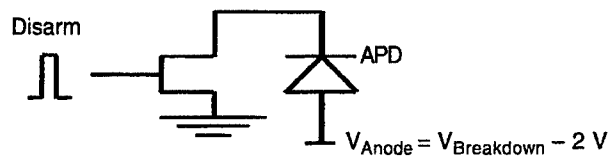


Figure 5-7. Quenching of APD by switching on n-FET with its drain connected to APD cathode.

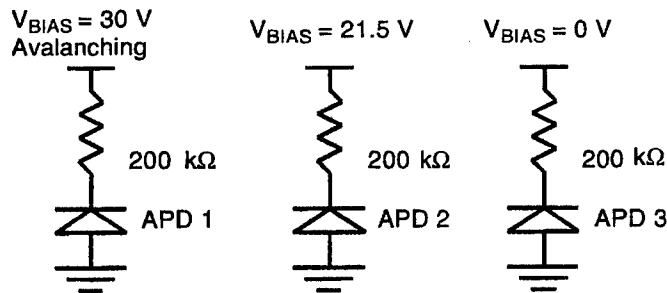


Figure 5-8. Three different reverse bias conditions at 100 K for irradiation of APDs. The APD breakdown voltage is ~ 25 V.

Low dark count rates indicate an APD that is less noisy, which is important for minimizing erroneous avalanches by thermal EHPs when the APD is armed. Optically and thermally generated avalanches are electronically indistinguishable from each other, so APDs with low dark count rates are needed to achieve high signal-to-noise ratios. The APD dark count rate serves, therefore, as a good figure of merit for comparing the performance of APD devices.

Proton radiation, with an energy of 40 MeV, from a cyclotron was used to irradiate devices. The first experiment irradiated APD devices with a dose of 1.5×10^{12} protons/cm², which is ~ 200 krad (Si). The second and third irradiations, of different devices, used a lower dose of 10^{12} protons/cm², or ~ 130 krad.

For the first experiment, we employed passive arming and quenching. The APDs were sawn from a wafer, packaged, and then placed in a cryostat. We avoided the use of active arming and quenching FET devices to simplify the irradiation and testing in the chilled state and to avoid irradiating the arming and quenching transistors.

In the initial experiment, we irradiated APDs under three different reverse bias conditions at 100 K, as shown in Figure 5-8. As a consequence of these applied voltages, one APD was avalanching during irradiation, one had a reverse bias voltage across the device terminals slightly below the breakdown voltage, and another had 0-V reverse bias maintained across the terminals. Dark count rate measurements were made on the APDs at 100 K prior to and after radiation exposure, while the APDs were maintained at 100 K to prevent annealing of radiation damage at room temperature. The results of this first experiment,

TABLE 5-1
Dark Count Rate of APDs Before and After Proton Irradiation at 100 K

	Reverse Bias Level During Irradiation (V)	Dark Count Rate at 100 K Before Irradiation (Hz)	Dark Count Rate at 100 K After Irradiation (kHz)
APD 1	30	50	92
APD 2	21.5	70	25.5
APD 3	0	61	17

TABLE 5-2
Dark Count Rate of Irradiated APDs After Room-Temperature Annealing

	Dark Count Rate After Irradiation and Room-Temperature Annealing (kHz)
APD 1	50.5
APD 2	46
APD 3	46

shown in Table 5-1, indicate the APD avalanching during radiation exposure experienced the greatest increase in dark count rate, and the APD biased at 0 V suffered the lowest increase.

After these measurements were taken, the APDs were allowed to anneal at room temperature for 4 days. Then measurements were taken again, and these data are shown in Table 5-2. It appeared that annealing at room temperature was insufficient to repair all the damage in the detector caused by the radiation. The increase in dark count rate for APDs 2 and 3 after annealing could be due to irradiation-induced shifts in junction breakdown voltage or, possibly, subtle changes in the measurement setup. Further measurements also indicated that the APD dark count rate did not change exponentially with $1/T$, where T is the absolute temperature. More measurements will be made to study this phenomenon.

In the second set of irradiations, we actively armed and quenched the APDs at 100 K to emulate the electronic environment of integrated readout circuits more closely. The circuit we used is shown in Figure 5-9. This time, however, we also measured APD devices whose cathode terminals were held in a high impedance state, i.e., there was no return path from the cathode to ground.

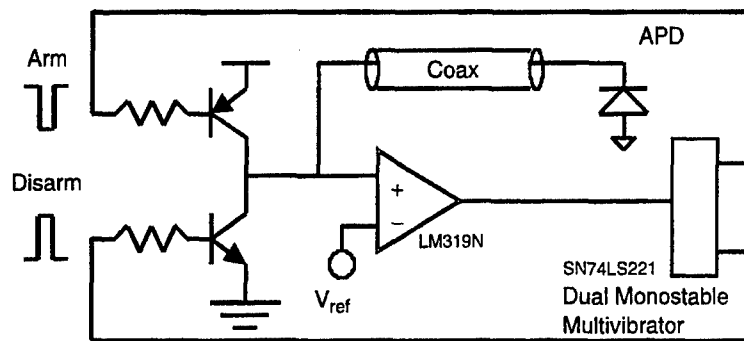


Figure 5-9. Circuit used in second set of irradiations in which APDs were actively armed and quenched to more closely emulate the electronic environment of integrated readout circuits.

Because of the increased capacitance of the coaxial cable, large dark count rates were observed in all devices. Nonetheless, it was possible to determine from data that the APDs that had their cathode at high impedance during irradiation had lower increases of dark count rates than any of the other devices that had their terminals connected by a 200-k Ω ballast resistor, including those held at 0-, 21.5-, or 30-V bias.

In the third irradiation set, devices at 100 K had their cathodes in a high impedance state and were probed and measured in a low-capacitance environment at the wafer level. Some annealing near room temperature did take place for these devices, but even so, data taken from the first irradiation run indicated that annealing at room temperature would not totally remove radiation damage. Figure 5-10 shows the circuit, microprobe, and cold wafer chuck used for making measurements on APDs during the third irradiation experiment.

Results are shown in Figure 5-11 for the third experiment for devices measured at room temperature, just 2 h after exposure to ionizing radiation at 100 K. APDs that have a cathode at high impedance during radiation exposure suffer relatively small increases in dark count rate. The dark count rates in Figure 5-11 reveal at 2.5-V overbias an increase from 12,000 to 16,000 counts per second. This is a relatively small increase compared to the APD in Figure 5-12, which was avalanching during irradiation and whose dark count rate increased at 2.5-V overbias from 20,000 to 50,000 dark counts per second (note change in ordinate scales). For an avalanching APD the dark count rate almost triples following exposure to ionizing radiation. This is significant compared to just a 33% increase in dark count rate for the APD of Figure 5-11, whose cathode was floating during ionizing radiation exposure of the same dose.

To gain some insight into exactly what specific radiation effects are responsible for damaging the APDs, we irradiated devices at room temperature with tungsten x-rays to a dose of 130 krads, with anode and cathode terminals floating. The data plots are shown in Figure 5-13. The results from those measurements indicate that x-ray radiation, which is ionizing but unlikely to cause bulk damage in silicon,



Figure 5-10. Circuit, microprobe, and cold wafer chuck used for measurements on APDs during the third irradiation experiment.

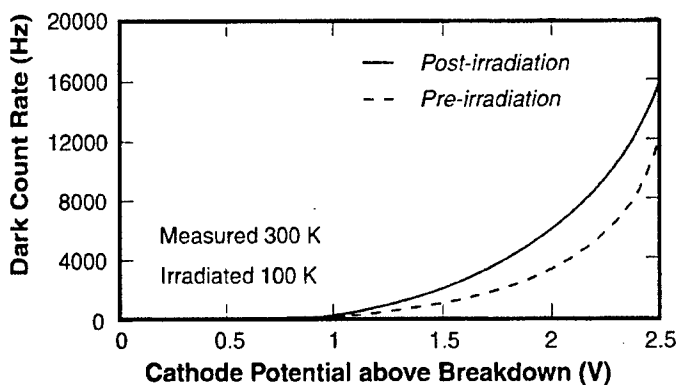


Figure 5-11. Pulsed dark count vs dc overbias potential for an APD irradiated with protons with its cathode held at high impedance.

does appear to contribute to APD damage. It should be emphasized that about 99.8% of the energy in a 40-MeV proton beam is ionizing, while only 0.2% contributes to bulk damage. The similarities between the proton and x-ray irradiations suggest the damage is limited to generation of surface or interface states. In an n^+p diode structure, as employed in the APDs, such interface states are most important at the perimeter of the device. No explicit attempt had been made in fabrication of the APDs to harden these interfaces, but a large body of knowledge exists on how such hardening might be accomplished.

The implications of the present results have significance in determining the best way to operate these devices in a harsh radiation environment. In light of the data, it would seem advantageous to have

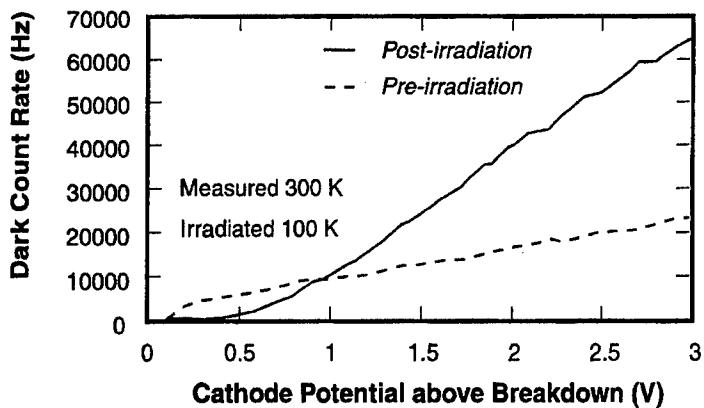


Figure 5-12. Dark count rate vs dc overbias potential for an APD that was avalanching during irradiation with protons.

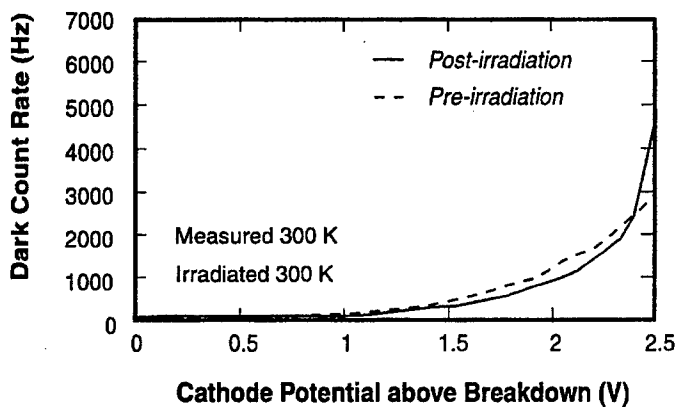


Figure 5-13. Pulsed dark count vs dc overbias potential for an APD before and after irradiation with x-rays.

redundant APD arrays on a focal plane array imager so that some devices could remain quiescent and only be activated after the risk of irradiation was deemed to be low.

A. Stern
J. A. Gregory

REFERENCES

1. B. E. Burke, J. A. Gregory, R. W. Mountain, B. B. Kosicki, E. D. Savoye, P. J. Daniels, V. S. Dolat, T. A. Lind, A. H. Loomis, and D. J. Young, in *Optical Detectors for Astronomy* (Kluwer, Boston, 1998), pp. 19-28.
2. B. E. Burke, J. A. Gregory, G. A. Luppino, J. L. Tonry, A. H. Loomis, C. C. Cook, D. J. Young, M. J. Cooper, and T. A. Lind, in *Optical Detectors for Astronomy II* (Kluwer, Boston, 2000), pp. 187-199.
3. T. A. Lind, R. K. Reich, W. H. McGonagle, and B. B. Kosicki, *Proc. SPIE* **3649**, 232 (1999).
4. B. F. Aull, *56th Annual Device Research Conference Digest* (IEEE, Piscataway, N.J., 1998), pp. 58-59.

6. ANALOG DEVICE TECHNOLOGY

6.1 NONLINEAR DIELECTRIC MICROWAVE LOSSES IN MgO SUBSTRATES

Understanding the nonlinearities in superconductive microwave devices is relevant for applications in communication systems, because narrow-band receive or high-power transmit filters can be susceptible to intermodulation distortion (IMD) or power-dependent absorption [1]–[3]. The sources of nonlinearities are not well understood at present, and several groups have reported unexpected features like the recovery of superconductivity [4]–[8] or noncubic power dependences of the third-order two-tone IMD or harmonic generation [9],[10].

We have measured the effective surface impedance $Z_{\text{eff}} = R_{\text{eff}} + jX_{\text{eff}}$ of several epitaxial $\text{YBa}_2\text{Cu}_3\text{O}_{7-\delta}$ (YBCO) films on MgO and observed a dramatic reduction of the power dissipation at microwave electric fields $E_{\text{ff}} \sim 100$ V/m below 20 K. The effective surface resistance is derived from the unloaded quality factor comprising losses in the superconductor and the dielectric and is given by

$$R_{\text{eff}} = R_s + G \times \tan \delta \quad (6.1)$$

where R_s is the surface resistance of the superconductor, $\tan \delta$ the loss tangent of the dielectric, and G a geometry factor, which depends on the ratio of penetration depth to film thickness [11], and hence, weakly on temperature ($G \sim 0.8 \Omega$ is typical for $T < T_c/2$). Changes of the effective reactance are similarly composed of changes of the penetration depth and dielectric permittivity

$$\Delta X_{\text{eff}} = \Delta X_s + G \times \frac{\Delta \epsilon}{\epsilon} \quad (6.2)$$

where $\Delta X_s = \mu_0 \omega \Delta \lambda$, λ is the temperature-dependent superconducting penetration depth, and ϵ the dielectric permittivity of the substrate.

Measurements on a Nb film on MgO have revealed the same behavior, while the anomalies were absent in both YBCO and Nb films on LaAlO_3 or CeO_2 -buffered sapphire. These results prove that the dielectric loss tangent of MgO causes the anomaly. Nonlinear dielectric losses, which can affect any microwave device application, have not been previously reported for MgO in the microwave range.

We describe representative results for one YBCO film with $T_c = 90.7$ K, critical current densities of 1.5 and 5.8 MA/cm^2 at $T = 77$ and 60 K, and $R_s = 60 \mu\Omega$ at $T = T_c/2$ and 2.3 GHz. Above 20 K, R_{eff} remained constant up to $I_{\text{ff}} = 0.5$ A, which corresponds to a magnetic flux density of about 15 mT. We observed similar results for all other YBCO films on MgO. The Nb films on MgO behaved similarly at low temperature but were limited to $T < 8$ K. The Nb films on sapphire showed no anomalous power dependence.

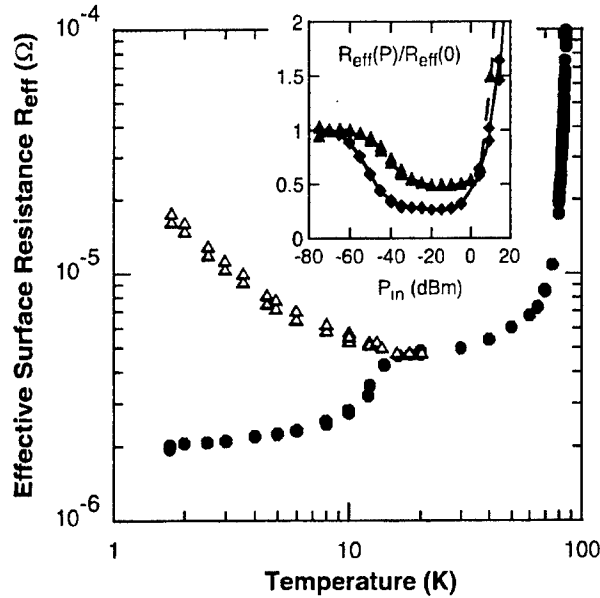


Figure 6-1. Temperature-dependent effective surface resistance of YBCO film at $\omega/2\pi = 2.3$ GHz, for two input power levels (-60 dBm, open triangles; -20 dBm, circles), corresponding to $E_{rf} \sim 0.5$ and 10^4 V/m. Note the logarithmic scales for illustration. The inset shows the normalized R_{eff} vs input power for the YBCO film (diamonds) and a Nb film on MgO (triangles) at $T = 5$ K. The absolute values of R_{eff} of both samples at 1.7 K were identical.

Figure 6-1 displays $R_{eff}(T)$ for the two power levels that produce extreme R_{eff} values. Below 20 K, $R_{eff}(T)$ decreases at the higher power and approaches $2 \mu\Omega$. This value is in accordance with high-quality epitaxial YBCO films and yields an upper limit for the loss tangent of $\approx 10^{-6}$, as expected for MgO at 20 K and 2.3 GHz [12],[13]. However, at low power, $R_{eff}(T)$ increases and becomes dominated by dielectric losses. The inset to Figure 6-1 shows very similar power dependences of R_{eff} for the two totally different superconductors YBCO and Nb, both on MgO, reinforcing the conclusion that dielectric loss in the MgO is responsible for the anomalous low-temperature behavior. Using $R_s \sim 2 \mu\Omega$ for YBCO and $R_{eff} \sim 20 \mu\Omega$, we derive $\tan \delta \approx 2 \times 10^{-5}$ at 1.7 K, which is 10–20 times above the value at 20 K. We are not aware of previous reports on $\tan \delta$ of MgO below 20 K.

Figure 6-2 summarizes typical results for the temperature dependence of ΔX_{eff} , measured for the same YBCO film as shown in Figure 6-1. Complementary to the loss tangent, the dielectric permittivity, monitored by changes of the effective surface reactance $\Delta X_{eff}(T)$, displayed a shallow minimum at $T \sim 5$ K but remained independent of power up to moderate power levels. Reflecting again the growing influence of $Z_d(T)$ on $Z_{eff}(T)$ at low temperatures, the increase of $\Delta X_{eff}(T)$ in Figure 6-2 can be entirely associated with the dielectric permittivity of MgO. Such an extremal behavior must not be confused with anomalous effects in the cuprate superconductor, which could be misinterpreted, e.g., as an indication of Andreev bound states at interfaces in d-wave superconductors [14].

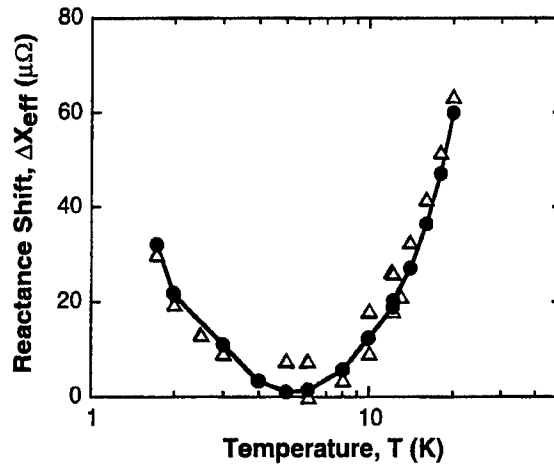


Figure 6-2. Typical data for shift of surface reactance at 2.3 GHz for YBCO on MgO at temperatures below 20 K for power levels shown in Figure 6-1 that give maximum change in effective surface resistance (-60 dBm, triangles; -20 dBm, circles).

The unique temperature and power dependences of the dissipative and reactive response of MgO helped us to identify the underlying mechanism. Very similar features were observed for amorphous glasses and highly disordered crystalline solids in similar ranges of frequency and temperature [15],[16]. The observed behavior was attributed to tunneling of atoms or molecules between nearly equivalent positions in the solid. This scientific area is subject to ongoing experimental and theoretical research [17]. Nevertheless, many features can be understood in the framework of a simple quantum mechanical two-level system. Phenomenologically, this model has similarities with the double-well potential underlying the Debye equations for dielectric relaxation [18]. The major difference between the two models is the resonant character of the transitions in the former in contrast to the relaxational character in the latter. Dielectric resonances of isolated defects usually occur in the submillimeter wave range or at even higher frequencies, but recent theoretical studies have shown that clustering of defects can reduce the resonant frequencies very strongly, so that they may even reach into the microwave range [19].

The temperature dependence of the loss tangent can be easily derived from Fermi's golden rule. The temperature dependence of the dielectric permittivity, then, follows from that of $\tan \delta$ through the Kramers-Kronig-relation, which requires additional information on the frequency range over which resonances occur. Different results have to be expected for solids with rather dilute defects, where the resonances remain sharp and limited to a well-defined frequency interval, and for highly disordered systems. According to [16], one gets

$$\text{an } \delta(T) = \frac{\pi}{\epsilon_0 \epsilon_r} \times n_d \mu^2 \times \tanh\left(\frac{hf}{2kT}\right) \quad (6.3)$$

for the dielectric loss tangent at low intensities, and

$$\frac{\Delta\epsilon_r(T)}{\epsilon_r} = -\frac{2}{\epsilon_0\epsilon_r} \times n_d\mu^2 \times \ln\left(\frac{T}{T_0}\right) \quad (6.4)$$

for the fractional change of the permittivity in highly disordered systems. In Equations (6.3) and (6.4), n_d and μ describe the density and the electric dipole moment of the defects.

The two-level model also explains in a natural way the anomalous power dependence, as resulting from saturation effects due to enhanced population of the higher energy level for increasing intensity of the microwave field. To derive the power dependence of the complex permittivity requires a more sophisticated mathematical framework, which bears similarities with the Bloch equations for a spin-1/2-particle in a magnetic field [15]:

$$\tan \delta(S_{\text{rf}}) = \tan \delta(0) \times \left(1 + \frac{S_{\text{rf}}}{S_0}\right)^{-1/2} \quad (6.5)$$

where S_{rf} denotes the intensity of the rf field, $S_{\text{rf}} \propto E_{\text{rf}}^2$, and the real part of the permittivity is independent of power. The threshold intensity S_0 depends on μ but not on n_d . It bears also information on the characteristic relaxation times of the excited defect states [16].

We compare our experimental results with the theoretical expectation in Figures 6-3 and 6-4. In Figure 6-3(a) we plot the difference between the two curves shown in Figure 6-1, normalized by G , vs the temperature function expected from Equation (6.3). We also include in this figure our results for a Nb film on MgO (diamonds). Both data sets are consistent with the expected linear relationship. The similar slopes indicate very similar properties, $n_d\mu^2$, of the MgO substrates, although these were bought from different suppliers. Figure 6-3(b) shows the corresponding result for the fractional variation of ϵ_r expected from Equation (6.4). The data derived for the YBCO film were not corrected for changes of the superconducting penetration depth, since $\lambda(T)$ can be safely assumed to be constant below 20 K. The situation is different for Nb with $T_c = 9.2$ K, where we accounted for $\Delta\lambda(T)$ according to BCS theory. As for the loss tangent, we find very similar results for both superconductors. The slopes in Figures 6-3(a) and 6-3(b), which should differ for a highly disordered system by a factor of $-\pi/2 \sim -1.6$, differ by $-5.5 \times 10^{-4} / 6.5 \times 10^{-5} \sim -8.5$. The difference of a factor of ~ 5 is attributed to the nature of the defects in a highly crystalline material like MgO.

A typical measured power dependence of $\tan \delta$ is compared with Equation (6.5) in Figure 6-4 for a YBCO film and a Nb film, both on MgO. The symbols represent the measured data, the curves denote the result of a single-parameter fit

$$R_{\text{eff}}(E_{\text{rf}}) = R_s + \Delta R_{\text{eff}} \times \left(1 + \frac{E_{\text{rf}}^2}{E_0^2}\right)^{-1/2} \quad (6.6)$$

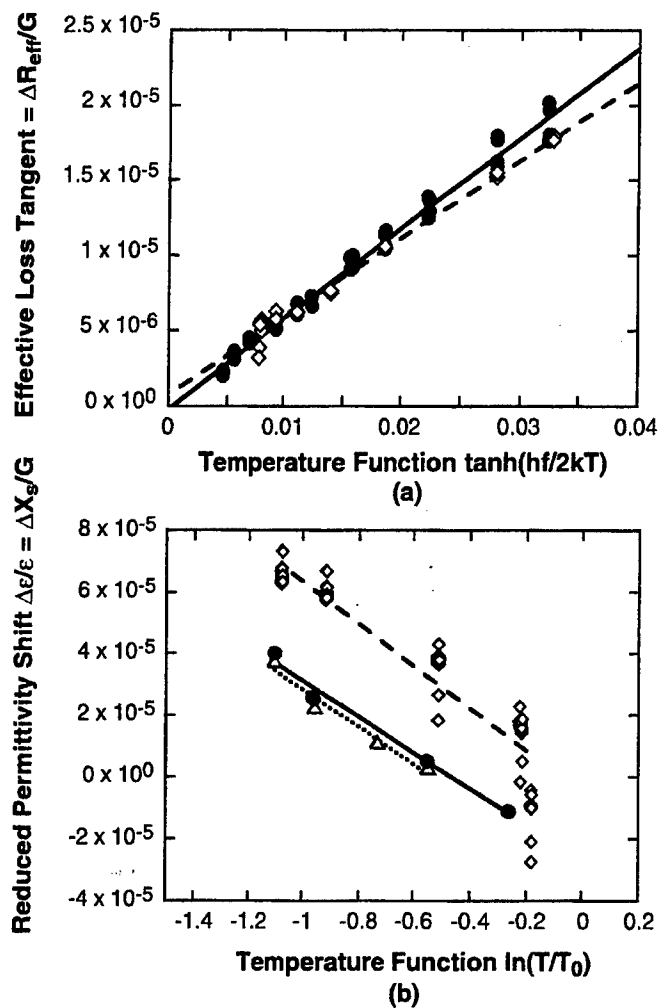


Figure 6-3. Temperature-dependent (a) dielectric loss tangent and (b) permittivity at $f = 2.3$ GHz for YBCO on MgO (-60 dBm, triangles, dotted interpolation; -20 dBm, circles, solid interpolation) and Nb on MgO (various power levels, diamonds, dashed interpolation), as expected for resonant absorption. $T_0 = 5.2$ K. The $\Delta X_{\text{eff}}(T)$ data for Nb were corrected for the temperature variation of the superconducting penetration depth according to the BCS theory ($T_c = 9.2$ K, $\Delta(0)/kT_c = 1.8$).

which is equivalent to Equation (6.5). The parameters R_s and ΔR_{eff} are given by the experimental data, while E_0 can be varied within a narrow range to optimize the fit. The data in Figure 6-4 indicate similar E_0 values for the two types of films on MgO substrates used, which implies similar types of defects. The ΔR_{eff} values for Nb/MgO seem a bit higher than for YBCO/MgO, which could hint of a larger defect density in the substrate.

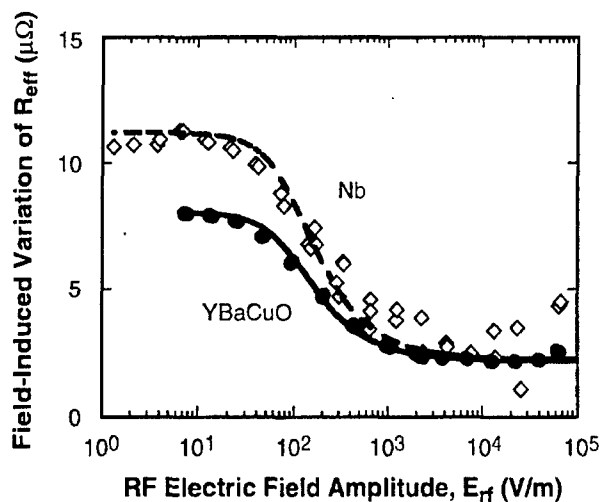


Figure 6-4. Electric field-induced variation of the effective surface resistance for YBaCuO (circles) and Nb (diamonds) on MgO at $f = 2.3$ GHz and $T = 5$ K. The dashed and solid curves denote fits to Equation (6.6).

To summarize, in MgO, at temperatures below 20 K, the dielectric loss tangent was found to dominate the nonlinear response of the resonators. The dissipation losses decreased with increasing power by up to one order of magnitude. This anomaly was accompanied by enhanced IMD. The surface reactance passed through a shallow minimum at about 5 K but remained independent of power. The results were very similar for all investigated YBaCuO films as well as for Nb films on MgO made for reference. We attribute these effects to resonant absorption by impurity states in MgO. While proper identification of the impurities is lacking at present, OH^{2-} ions are considered the most likely candidates, since they are greatly abundant in melt-fused MgO.

D. E. Oates	M. A. Hein*
P. J. Hirst*	R. G. Humphreys*
A. V. Velichko*	

REFERENCES

1. N. Newman and W. G. Lyons, *J. Supercond.* **6**, 119 (1993).
2. H. J. Chaloupka, in *Applications of Superconductivity*, H. Weinstock, ed., in *Nato Science Series: B Physics* (Kluwer, Dordrecht, 2000).

*Author not at Lincoln Laboratory.

3. O. G. Vendik and I. B. Vendik, *IEEE Trans. Microw. Theory Tech.* **45**, 173 (1997); **46**, 851 (1998).
4. D. P. Choudhury, B. A. Willemsen, J. S. Derov, and S. Sridhar, *IEEE Trans. Appl. Supercond.* **7**, 1260 (1997).
5. M. A. Hein, A. Cassinese, S. Hensen, T. Kaiser, G. Müller, and M. Perpect, *J. Supercond.* **12**, 129 (1999).
6. A. P. Kharcl, A. V. Velichko, J. R. Powell, A. Porch, M. J. Lancaster, and R. G. Humphreys, *Phys. Rev. B* **58**, 11189 (1998).
7. P. Lahl and R. Wördenweber, private communication.
8. K. Irgmaier, private communication.
9. B. A. Willemsen, K. E. Kihlstrom, and T. Dahm, *Appl. Phys. Lett.* **74**, 753 (1999).
10. J. C. Booth, L. R. Vale, and R. H. Ono, *IEEE Trans. Appl. Supercond.* **11**, 1387 (2001).
11. D. M. Sheen, S. M. Ali, D. E. Oates, R. S. Withers, and J. A. Kong, *IEEE Trans. Appl. Supercond.* **1**, 108 (1991).
12. J. Krupka, R. G. Geyer, M. Kuhn, and J. H. Hinken, *IEEE Trans. Microw. Theory Tech.* **42**, 1886 (1994).
13. T. Konaka, M. Sato, H. Asano, and S. Kubo, *J. Supercond.* **4**, 283 (1991).
14. H. Walter, W. Prusseit, R. Semerad, H. Kinder, W. Assmann, H. Huber, H. Burkhardt, D. Rainer, and J. A. Sauls, *Phys. Rev. Lett.* **80**, 3598 (1998); A. Carrington, F. Manzano, R. Prozorov, R. W. Giannetta, N. Kameda, and T. Tamegai, *Phys. Rev. Lett.* **86**, 1074 (2001).
15. S. Hunklinger and M. von Schickfus, in *Amorphous Solids*, W. A. Phillips, ed. (Springer, New York, 1981), pp. 81-105.
16. U. Strom, M. von Schickfus, and S. Hunklinger, *Phys. Rev. Lett.* **41**, 910 (1978).
17. S. Hunklinger and C. Enss, in *Insulating and Semiconducting Glasses*, P. Boolchand, ed., Vol. 17 of *Series of Directions in Condensed Matter Physics* (World Scientific, Singapore, 2000), p. 499.
18. V. V. Daniel, *Dielectric Relaxation* (Academic, New York, 1967).
19. M.W. Klein, *Phys. Rev. B* **40**, 1918 (1989).

**This Page Intentionally
Left Blank**

7. ADVANCED SILICON TECHNOLOGY

7.1 "GRATEFUL" PHASE SHIFT LITHOGRAPHY METHOD AS A COST-EFFECTIVE ALTERNATIVE FOR LOW-VOLUME LITHOGRAPHY NEEDS

Our previous resolution-enhanced lithography research focused on the formation of deeply scaled isolated gate features for enabling advanced silicon-on-insulator device research [1]. This work was based on implementation of double-exposure phase shift imaging methods [2],[3]. In this new study, the application of multiple exposure strong phase shift lithography to fully scaled low-volume circuit patterns was explored, using a dense-only patterning method dubbed "GRATEFUL" (Gratings of Regular Arrays and Trim Exposures For ULSI Lithography) [4],[5]. Such an approach offers the benefits of reduced mask complexity and design cycle time, at the expense of decreased process throughput and limited design flexibility. In particular, dense-only methods offer $k_1 < 0.3$, thus enabling 90-nm node lithography with high numerical aperture 248-nm exposure systems (resolution = $k_1 \lambda / NA$). Optical proximity and related spatial frequency limitations of subwavelength lithography are mitigated using this method. The high mask costs associated with phase shift technology are minimized by the ability to re-use the dense phase shift "master" template masks many times for different circuit designs.

Through experiments and simulation, the trade-offs inherent in dense-only template phase shift lithography were explored. Gate and contact patterns corresponding to various fully scaled circuits were demonstrated. A particular focus of this work was the formation of deeply scaled dense and isolated gate features in both the horizontal and vertical orientation. This effort was directed toward addressing the economic challenges that optical lithography extension technologies present for low-volume applications such as defense. This challenge is also faced in the commercial semiconductor sector in which advanced resolution-enhancement techniques (RETs) are only economically feasible for very high volume applications such as memories and microprocessors. Other important applications, such as application-specific integrated circuits (ASICs), system-on-a-chip (SOC) circuits, analog-rf circuits, and photonics, cannot justify the cost of advanced RET technology. In this sense, the GRATEFUL method can be thought of as an alternative to maskless lithography approaches for low-volume, high-performance, semiconductor circuit fabrication requirements.

In its least complex form, the phase shift template mask used by GRATEFUL is a simple one-dimensional grating. A schematic of the process is shown in Figure 7-1. A dense grating phase shift mask is first imaged, followed by a second exposure to trim undesired features. This double exposure process forms a series of narrow line segments on the wafer. At this point the resist is hard baked and a second layer of resist coated on the wafer. For cases where the fine features are oriented in only one direction, the gate interconnect is formed in this second layer of resist. If fine features are desired in both orientations, the dense grating and trim exposures are performed in this second layer of resist. Alternatives to the double resist process described here include the use of a hardmask or double bilayer resist.

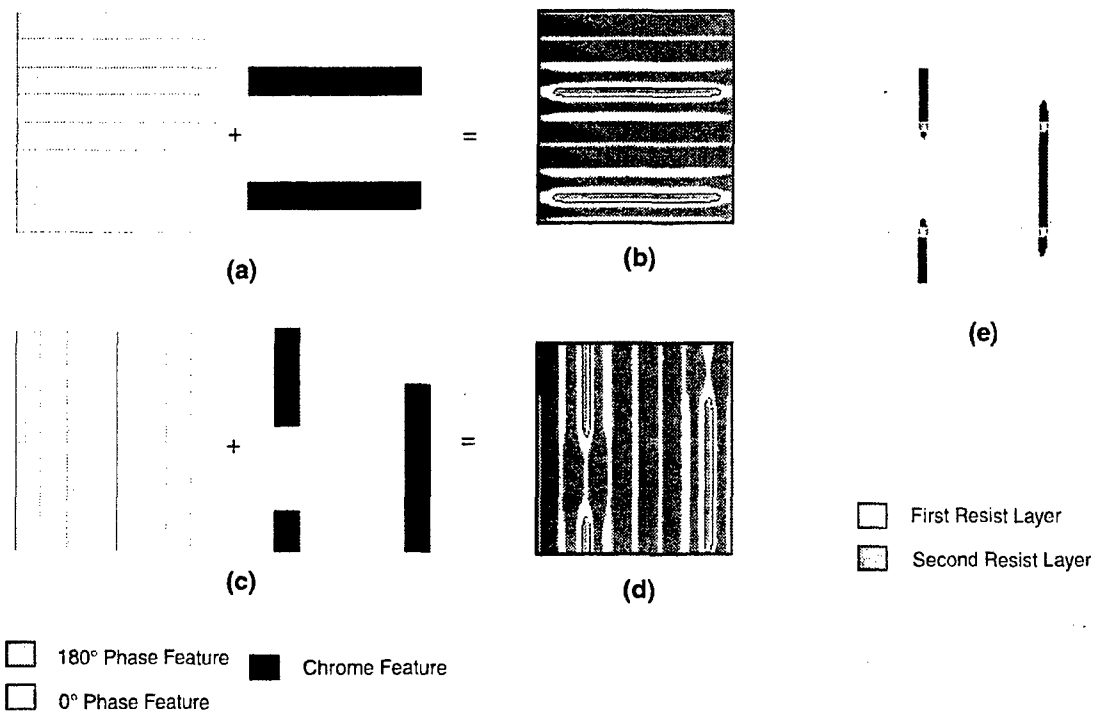


Figure 7-1. Schematic diagram of the GRATEFUL imaging method: (a) horizontal phase shift and trim masks, (b) simulated first resist image (relative total exposure dose), (c) vertical phase shift and trim masks, (d) simulated second resist image (relative total exposure dose), and (e) geometric union of horizontal and vertical resist features (simple resist threshold model). Simple phase shift template masks are used for the fine feature definitions.

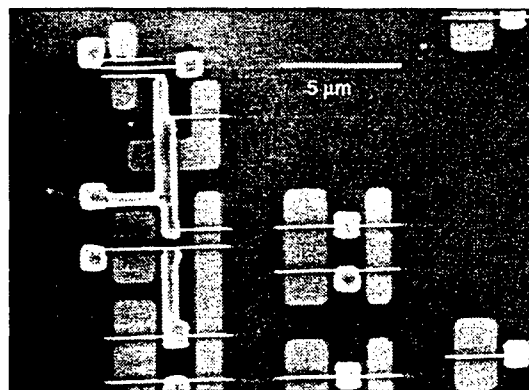


Figure 7-2. Experimental example of circuit pattern imaged using GRATEFUL. All the fine features are in one orientation in this example so only three exposures were required. Note the absence of optical proximity effects for these 65-nm gate features imaged through pitch values of 250 nm to isolated.

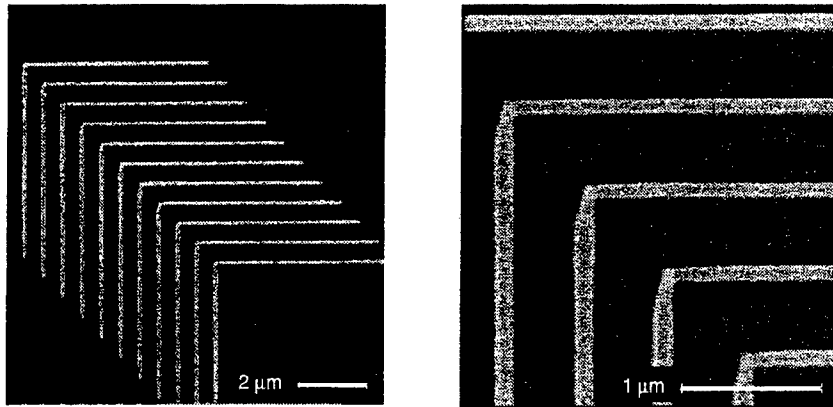


Figure 7-3. Experimental example of two-dimensional test pattern imaged using GRATEFUL. The x -oriented features are 85 nm and the y -oriented features 125 nm. Note the sharp corners achieved through the use of two optically independent resist layers.

An experimental example of the GRATEFUL method applied to a circuit pattern is shown in Figure 7-2. In this case all fine features are oriented in the same (horizontal) direction. Three exposures were required here: phase shift mask grating, trim, and interconnect. Note the absence of optical proximity effects indicated by the excellent critical dimension (CD) control for fine features through pitch. The pitch range for this pattern ranged from 250 nm to isolated. The lithography was performed using a dense one-dimensional phase shift grating mask, and conventional trim and interconnect masks. A Canon EX-4, 248-nm stepper was used with a numerical aperture (NA) of 0.6. This resolution meets the requirements of the current 130-nm node for microprocessor lithography using a lithography tool of 1998–1999 vintage. In addition, the mask used was much simpler than most current implementations of 130-nm node lithography.

Examples of GRATEFUL applied to patterns with fine features in both the x and y orientations are shown in Figures 7-3 and 7-4. A test pattern is shown in Figure 7-3 with fine features in both orientations. A different dose was used for the two phase shift mask exposures resulting in different sizes for the features in each orientation. Since the x and y fine features were formed in *different optically independent* layers of resist, it was possible to form sharp corners that would normally be difficult in a single layer of resist because of spatial frequency limitations. A two-dimensional grid pattern formed in two layers of photoresist is shown in Figure 7-4.

A more complex circuit example (a full adder) with fine features in both orientations is shown in Figure 7-5. This design was simulated using lithography simulation software from Numerical Technologies (IC Workbench). Such simulation software is becoming more common to verify subwavelength lithography processes, since the mask no longer resembles the final circuit pattern.

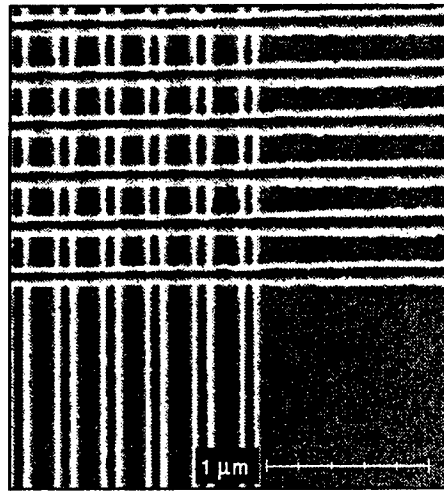


Figure 7-4. Two-dimensional grid pattern fabricated in two layers of resist. Such a method is capable of producing very sharp corner features for low values of k_1 . The grating pitch value is 280 nm in this case.

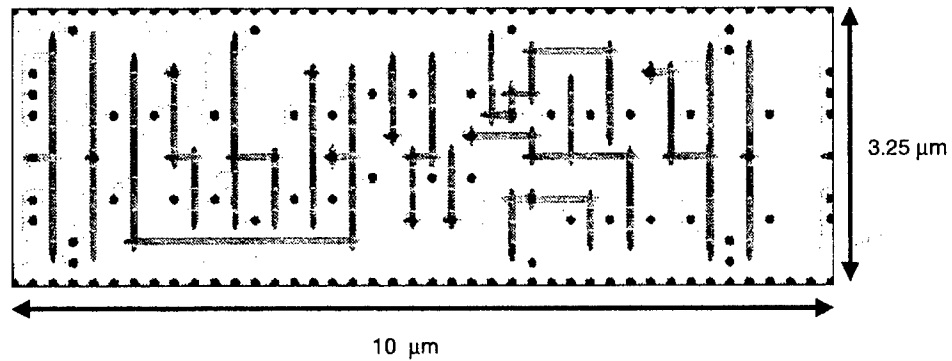


Figure 7-5. Simulated thresholded aerial image plot of a full adder circuit implemented using GRATEFUL. This implements a $k_1 = 0.3$ lithography process for our Canon EX-4, 248-nm stepper with numerical aperture 0.6. Simulations were performed using Numerical Technologies' IC Workbench software.

Figure 7-5 shows the aerial image intensity patterns from the four exposures required to make this pattern. Part of this circuit pattern is shown in the experimental example in Figure 7-6. Note the fine features in both orientations formed in the two layers of resist. A key challenge of the double resist process was the control of reflections for the second resist layer since the hardbake of the first resist layer thinned the organic antireflection film we employed for this purpose.

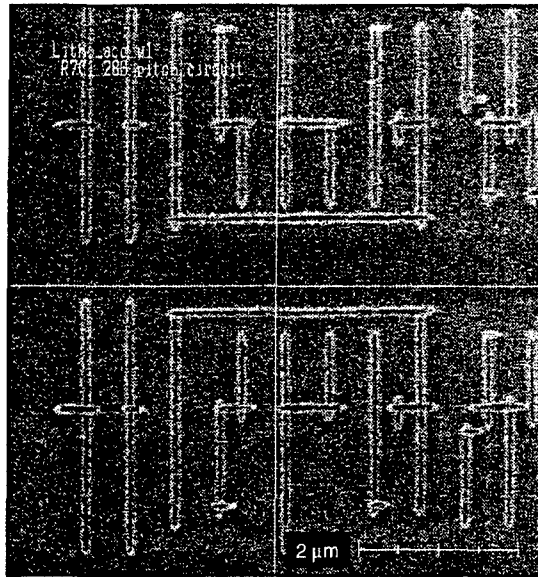


Figure 7-6. Experimental example of full adder circuit region imaged using GRATEFUL. Note the fine features oriented in x and y directions imaged using the same one-dimensional phase shift mask grating.

When using the phase shift mask templates, it is often desirable to print a variety of near minimum width features in the final circuit pattern. This can be accomplished in several ways. The conventional trim mask can include graytone features that act to locally modify the CD of the fine line features [6]. Multiplex or subthreshold exposures can also be used alone or in combination with graytone trim features in order to enable the imaging of multiple fine feature CDs using the GRATEFUL method [7].

In summary, we have studied a new lithography method GRATEFUL. This method sacrifices process complexity and design flexibility to gain dramatically lower mask cost. In addition, optical proximity and related spatial frequency effects are minimized using this method. These effects are becoming quite difficult to control using conventional proximity correction methods. Designs must place fine features at integral multiples of a dense grid. We believe that this imaging approach can make advanced resolution-enhanced optical lithography practical for low-volume applications such as defense, ASICs, SOC circuits, analog-rf circuits, and photonics. In these important cases the trade-offs inherent in GRATEFUL may make sense. This type of lithography approach can also be thought of as an alternative to maskless methods currently being pursued.

M. Fritze
R. Mallen

B. Tyrrell
B. Wheeler

REFERENCES

1. Solid State Research Report, Lincoln Laboratory, MIT, 2000:1, p. 61.
2. H. Y. Liu, L. Karklin, Y. T. Wang, and Y. C. Pati, *Proc. SPIE* **3334**, 2 (1998).
3. M. Fritze, J. Burns, P. W. Wyatt, C. K. Chen, P. Gouker, C. L. Chen, C. Keast, D. Astolfi, D. Yost, D. Preble, A. Curtis, P. Davis, S. Cann, S. Denault, and H. Y. Liu, *J. Vac. Sci. Technol. B* **18**, 2886 (2000).
4. M. Fritze, B. Tyrrell, D. Astolfi, D. Yost, P. Davis, B. Wheeler, R. Mallen, J. Jarmolowicz, S. Cann, D. Chan, P. Rhyins, C. Carney, J. Ferri, and B. A. Blachowicz, *J. Vac. Sci. Technol. B* **19**, 2366 (2001).
5. B. Tyrrell, M. Fritze, R. Mallen, B. Wheeler, P. Rhyins, and P. Martin, *Proc. SPIE* **4692**, 503 (2002).
6. M. Fritze, B. Tyrrell, R. Mallen, B. Wheeler, P. Rhyins, P. Martin, to be published in *J. Vac. Sci. Technol.* Nov.-Dec. 2002.
7. A. Suzuki, K. Saitoh, and M. Yoshii, *Proc. SPIE* **3679**, 396 (1999).

REPORT DOCUMENTATION PAGE

Form Approved
OMB No. 0704-0188

Public reporting burden for this collection of information is estimated to average 1 hour per response, including the time for reviewing instructions, searching existing data sources, gathering and maintaining the data needed, and completing and reviewing the collection of information. Send comments regarding this burden estimate or any other aspect of this collection of information, including suggestions for reducing this burden, to Washington Headquarters Services, Directorate for Information Operations and Reports, 1215 Jefferson Davis Highway, Suite 1204, Arlington, VA 22202-4302, and to the Office of Management and Budget, Paperwork Reduction Project (0704-0188), Washington, DC 20503.

1. AGENCY USE ONLY (Leave blank)	2. REPORT DATE 15 August 2002	3. REPORT TYPE AND DATES COVERED Quarterly Technical Report, 1 February -30 April 2002	
4. TITLE AND SUBTITLE Solid State Research		5. FUNDING NUMBERS C — F19628-00-C-0002	
6. AUTHOR(S) David C. Shaver		7. PERFORMING ORGANIZATION NAME(S) AND ADDRESS(ES) Lincoln Laboratory, MIT 244 Wood Street Lexington, MA 02420-9108	
9. SPONSORING/MONITORING AGENCY NAME(S) AND ADDRESS(ES) HQ Air Force Materiel Command AFMC/STSC Wright-Patterson AFB, OH 45433-5001		8. PERFORMING ORGANIZATION REPORT NUMBER 2002:3	
11. SUPPLEMENTARY NOTES None		10. SPONSORING/MONITORING AGENCY REPORT NUMBER ESC-TR-2002-077	
12a. DISTRIBUTION/AVAILABILITY STATEMENT Approved for public release; distribution is unlimited.		12b. DISTRIBUTION CODE	
13. ABSTRACT (Maximum 200 words) <p style="text-align: center;">This report covers in detail the research work of the Solid State Division at Lincoln Laboratory for the period 1 May-31 July 2002. The topics covered are Quantum Electronics, Electro-optical Materials and Devices, Submicrometer Technology, Biosensor and Molecular Technologies, Advanced Imaging Technology, Analog Device Technology, and Advanced Silicon Technology. Funding is provided by several DoD organizations—including the Air Force, Army, DARPA, MDA, Navy, NSA, and OSD—and also by the DOE, NASA, and NIST.</p>			
14. SUBJECT TERMS quantum electronics biosensor technology miniature laser system avalanche photodiode electro-optical devices molecular technology microlens fabrication phase shift lithography materials research advanced imaging technology photolithography submicrometer technology analog device technology charge-coupled device imager			15. NUMBER OF PAGES 66
17. SECURITY CLASSIFICATION OF REPORT Unclassified			16. PRICE CODE
18. SECURITY CLASSIFICATION OF THIS PAGE Same as Report	19. SECURITY CLASSIFICATION OF ABSTRACT Same as Report	20. LIMITATION OF ABSTRACT Same as Report	